

This discussion paper is/has been under review for the journal Atmospheric Chemistry and Physics (ACP). Please refer to the corresponding final paper in ACP if available.

Global NO_x emission estimates derived from an assimilation of OMI tropospheric NO₂ columns

K. Miyazaki^{1,2}, H. J. Eskes¹, and K. Sudo^{2,3}

¹Royal Netherlands Meteorological Institute (KNMI), Wilhelminalaan 10, 3732 GK, De Bilt, The Netherlands

²Japan Agency for Marine-Earth Science and Technology, Yokohama 236-0001, Japan

³Graduate School of Environmental Studies, Nagoya University, Nagoya, Japan

Received: 4 October 2011 – Accepted: 18 November 2011 – Published: 2 December 2011

Correspondence to: K. Miyazaki (miyazaki@knmi.nl)

Published by Copernicus Publications on behalf of the European Geosciences Union.

Title Page

Abstract

Introduction

Conclusions

References

Tables

Figures

◀

▶

◀

▶

Back

Close

Full Screen / Esc

Printer-friendly Version

Interactive Discussion



Abstract

A data assimilation system has been developed to estimate global nitrogen oxides (NO_x) emissions using OMI tropospheric NO_2 columns (DOMINO product) and a global chemical transport model (CTM), CHASER. The data assimilation system, based on an ensemble Kalman filter approach, was applied to optimize daily NO_x emissions with a horizontal resolution of 2.8° during the years 2005 and 2006. The background error covariance estimated from the ensemble CTM forecasts explicitly represents non-direct relationships between the emissions and tropospheric columns caused by atmospheric transport and chemical processes. In comparison to the a priori emissions based on bottom-up inventories, the optimized emissions were higher over Eastern China, the Eastern United States, Southern Africa, and Central-Western Europe, suggesting that the anthropogenic emissions are mostly underestimated in the inventories. In addition, the seasonality of the estimated emissions differed from that of the a priori emission over several biomass burning regions, with a large increase over Southeast Asia in April and over South America in October. The data assimilation results were validated against independent data: SCIAMACHY tropospheric NO_2 columns and vertical NO_2 profiles obtained from aircraft and lidar measurements. The emission correction greatly improved the agreement between the simulated and observed NO_2 fields; this implies that the data assimilation system efficiently derives NO_x emissions from concentration observations. We also demonstrated that biases in the satellite retrieval and model settings used in the data assimilation largely affect the magnitude of estimated emissions. These dependences should be carefully considered for better understanding NO_x sources from top-down approaches.

1 Introduction

Nitrogen oxides (NO_x) are important atmospheric species that affect atmospheric chemistry, air quality, and climate (IPCC, 2007). NO_x dominantly controls the

ACPD

11, 31523–31583, 2011

Global NO_x emissions

K. Miyazaki et al.

Title Page

Abstract

Introduction

Conclusions

References

Tables

Figures

◀

▶

◀

▶

Back

Close

Full Screen / Esc

Printer-friendly Version

Interactive Discussion



**Global NO_x
emissions**

K. Miyazaki et al.

Title Page

Abstract

Introduction

Conclusions

References

Tables

Figures

◀

▶

◀

▶

Back

Close

Full Screen / Esc

Printer-friendly Version

Interactive Discussion



5 tropospheric ozone (O₃) budget, the abundance of the hydroxyl radical (OH), and the formation of nitrate aerosol. The reactions between NO_x and hydrocarbons are major sources of O₃ in the troposphere. Tropospheric O₃ acts as a greenhouse gas and influences the lifetime of other greenhouse gasses. NO₂ also produces nitric acid (HNO₃)
10 by reacting with OH, forming nitrate aerosols and acid particles. NO_x has both anthropogenic and natural sources. Anthropogenic sources of NO_x include fossil fuel and biofuel combustion, mainly emitted from power plants, transport (automobiles, ships, and aircrafts), and industry. Natural sources of NO_x include soil, biomass burning, and lightning emissions. Dominant sinks of NO_x in the troposphere are gas-phase formations of HNO₃ through reaction of NO₂ with OH especially during daytime and aerosol uptake of NO₂, NO₃, and N₂O₅. The lifetime of NO_x is of the order of hours to days in the troposphere depending on various factors, including OH concentrations and photolysis rate (e.g., Lamsal et al., 2010). The short lifetime and the inhomogeneous source distribution of NO_x result in obvious spatiotemporal variations in the NO₂ concentration in the troposphere.

15 Bottom-up NO_x emission inventories from different sources and regions have large uncertainties. The extent of emission-related activities and emission factors used in the inventories are sources of error. Emission inventory information is often only available on a coarse resolution, such as country totals. In addition, simple multiplication factors
20 are sometimes supplied with the emissions to describe the diurnal, weekly and seasonal dependence in an average way. Moreover, many emission sources have a large diurnal, weekly, or seasonal variability that is often poorly represented in the inventories. Examples are the traffic rush hour, wintertime heating of buildings (e.g., Streets et al., 2003), biomass burning events and their mid-day maximums, and the seasonality and pulses of soil emissions triggered by rainfall (e.g., Velders et al., 2001; Wang et al., 2007).

25 Observations of NO₂ concentrations provide important information on NO_x emissions. Satellite retrievals provide better spatial coverage than in situ measurements, which can provide constraints on estimates of surface emissions. NO₂ can be

**Global NO_x
emissions**

K. Miyazaki et al.

[Title Page](#)[Abstract](#)[Introduction](#)[Conclusions](#)[References](#)[Tables](#)[Figures](#)[◀](#)[▶](#)[◀](#)[▶](#)[Back](#)[Close](#)[Full Screen / Esc](#)[Printer-friendly Version](#)[Interactive Discussion](#)

measured as a column integral from solar backscatter instruments from space, since it absorbs light in the visible portion of the electromagnetic spectrum. Because the satellite signal is closely related to the total amount of NO₂, there is a more direct link with area-averaged emissions than for surface in situ observations which depend strongly on local sources and local removal processes. Tropospheric NO₂ columns retrieved from satellite measurements, e.g., by Global Ozone Monitoring Experiment (GOME), GOME-II, Scanning Imaging Absorption Spectrometer for Atmospheric Cartography (SCIAMACHY), and Ozone Monitoring Instrument (OMI), have contributed to map spatiotemporal variations in NO_x sources (e.g., Martin et al., 2003; Richter, 2004; Van der A et al., 2006; Boersma et al., 2008; Stavrou et al., 2008; Kurokawa et al., 2009; Zhao and Wang, 2009; Lin et al., 2010). For instance, analyses of satellite data have identified rapid increases in NO_x emissions over developing areas (e.g., Richter, 2004; Van der A et al., 2006, 2008).

Top-down approaches adjust the emissions to reduce the discrepancy between the model and observation, while taking the errors in both model and retrievals into account. Martin et al. (2003) scaled bottom-up emissions directly based on the ratio of the local retrieved and model simulated columns. This approach has been widely applied to satellite retrievals owing to its simple implementation (e.g., Boersma et al., 2008; Zhao and Wang, 2009; Lamsal et al., 2010). However, changes in emissions are not necessarily proportional to the local column changes because of atmospheric processes. For example, the NO₂/NO_x ratio can vary owing to transport and chemical processes. To take these processes into account, recent studies have employed advanced data assimilation techniques including inverse modelling and four-dimensional variational assimilation (4-D-VAR) (Muller and Stavrou, 2005; Kurokawa et al., 2009; Chai et al., 2009). An ensemble Kalman filter (EnKF) is also an advanced data assimilation technique (Evensen, 1994; Hunt et al., 2007) in which the forecast error covariance is advanced by the model itself (i.e., flow-dependent forecast error covariance). These advanced approaches allow to fully take advantage of the chemical transport model (CTM). To the best of the authors' knowledge, no published research has yet

been conducted to estimate global NO_x emissions using EnKF to date.

In this study, we apply an EnKF data assimilation system to estimate daily global NO_x emissions using OMI satellite retrievals and the Chemical Atmospheric GCM for Study of Atmospheric Environment and Radiative Forcing (CHASER) CTM (Sudo et al., 2002b). Using the data assimilation, we investigate the global distribution and the seasonal variation of surface NO_x emissions. Even with such an advanced assimilation approach, however, the quality of both the model and the satellite retrieval will affect the accuracy of emission estimates (e.g., Van Noije et al., 2006; Lamsal et al., 2010). Therefore, we will discuss the impact of model settings and biased in the satellite retrievals on the estimated emissions. The methodology is described in Sect. 2. The performance of the CTM is validated against satellite retrievals and presented in Sect. 3. An optimal data assimilation setting for NO_x emission estimations will be discussed in Sect. 4. Data assimilation and validation results against independent observations are presented in Sect. 5. The sensitivity of emission estimates to model settings and satellite retrieval are investigated in Sect. 6. Concluding remarks and discussions are provided in Sect. 7.

2 Methodology

Daily OMI tropospheric NO₂ column observations are used to constraint NO_x emissions. The model simulation and assimilation results are validated using independent data, tropospheric NO₂ columns from SCIAMACHY measurements and vertical profiles obtained during the INTEX-B and the DANDELIONS campaigns. In this section, we introduce the model, the satellite data used in the assimilation, and the validation data sets.

Global NO_x emissions

K. Miyazaki et al.

Title Page

Abstract

Introduction

Conclusions

References

Tables

Figures

◀

▶

◀

▶

Back

Close

Full Screen / Esc

Printer-friendly Version

Interactive Discussion



2.1 Satellite and aircraft data

2.1.1 OMI data

The Dutch–Finnish OMI instrument, launched aboard the Aura satellite in July 2004, is a nadir viewing imaging spectrograph (Levelt et al., 2006). Aura traces a sun-synchronous, polar orbit with a period of 100 min. The local equator crossing time of Aura is about 13:40. OMI provides measurements of both direct and atmosphere-backscattered sunlight in the ultraviolet-visible range from 270 to 500 nm, that is used to retrieve tropospheric NO₂ columns. OMI pixels are 13 km × 24 km at nadir, increasing in size to 24 km × 135 km for the largest viewing angles. OMI retrievals with its daily global coverage are effective to constraint global NO_x emissions on a daily basis, different from GOME and SCIAMACHY retrievals with poorer spatial and temporal resolutions and less global coverage.

The Dutch OMI tropospheric NO₂ (DOMINO) data product (Boersma et al., 2007) is used in this study. The DOMINO product is provided by the Tropospheric Emission Monitoring Internet Service (TEMIS) data portal (www.temis.nl). Since the sensitivity of nadir measurements varies with height, a priori vertical profile and averaging kernel (AK) information are important in the retrieval and for the use of the observations in data assimilation (Eskes and Boersma, 2003). Detailed retrieval information is provided in DOMINO product, which allows proper use of observational information in data assimilation (cf., Sect. 2.3.1).

In the retrieval, the tropospheric air mass factors (AMFs) are computed at the time and location of the OMI overpass. The AMF measures the ratio of the slant column abundance to the vertical column abundance calculated from measured radiances with a radiative transport model. The AMF is determined by many factors; e.g., solar and viewing zenith angles, cloud fraction and cloud pressure derived using O₂-O₂ absorption, surface reflectivity, the a priori NO₂ profile simulated by a CTM, and the vertically resolved sensitivity to NO₂ of the solar radiation backscatter to space. Details of the retrieval and error estimates are described in Boersma et al. (2004). Meanwhile, the

Title Page

Abstract

Introduction

Conclusions

References

Tables

Figures

◀

▶

◀

▶

Back

Close

Full Screen / Esc

Printer-friendly Version

Interactive Discussion



**Global NO_x
emissions**

K. Miyazaki et al.

Title Page

Abstract

Introduction

Conclusions

References

Tables

Figures

◀

▶

◀

▶

Back

Close

Full Screen / Esc

Printer-friendly Version

Interactive Discussion



retrieved tropospheric NO₂ column error is derived from errors in total slant column, its stratospheric portion, and the tropospheric AMF (Boersma et al., 2004, 2007). The error is dominated by the AMF calculation over polluted area, whereas it is dominated by spectral fitting and stratosphere-troposphere separation over remote areas (Boersma et al., 2007). Only observations with a radiance reflectance of less than 50 % from clouds (i.e., cloud fraction less than about 20 %) are used in this study.

DOMINO v.1.03 data (hereafter DOMINO v1) released in 2008 generally shows good agreement with independent data, but appears to have a bias between 0 and 40 % (Boersma et al., 2011). Errors in the AMF may lead to high values for the AK and errors in the retrieval (Boersma et al., 2004, 2007; Lamsal et al., 2010). Boersma et al. (2011) describes improvements in the OMI retrieval, from DOMINO v1 to DOMINO v2.01 (hereafter DOMINO v2). The improvements include the description of the radiative transfer for the lowest atmospheric layers, assumptions made on surface albedo, terrain height, clouds, and sampling in a priori NO₂ profile. Tropospheric NO₂ columns retrieved from DOMINO v2 are about 20 % (10 %) lower in winter (in summer) compared to those from DOMINO v1 over polluted regions. We mainly use DOMINO v2 data to constrain NO_x emissions.

2.1.2 SCIAMACHY data

SCIAMACHY was launched in March 2002 on board ENVISAT (Bovensmann et al., 1999). We use tropospheric NO₂ data from the KNMI retrieval algorithm and the observation data were obtained from the TEMIS data server (Boersma et al., 2004). The ground pixel of the nadir mode is generally 60 by 30 km², with a global coverage approximately once every six days. The local overpass time is 10:00 a.m. The approach to calculate the AMF is almost the same as that for DOMINO v1 data, while DOMINO v2 is a major update with several changes to the AMF computation. Errors in the slant column fitting, the stratospheric corrections, and in the AMFs lead to an overall error in the SCIAMACHY retrieval, as described in Boersma et al. (2004). The retrieval was validated against in situ and aircraft measurements, and was compared with regional

air quality models (e.g., Schaub et al., 2007; Blond et al., 2007).

As discussed by Boersma et al. (2007) and Lin et al. (2010), systematic errors in OMI (DOMINO v1) and SCIAMACHY retrievals are expected to correlate well with each other, since these retrievals are derived with a very similar algorithm. Differences between OMI and SCIAMACHY retrievals thus mainly reflect temporal (diurnal) variations of chemical processes and emissions. As an exception, the improvements in DOMINO v2 may create systematic differences between the DOMINO v2 and the SCIAMACHY retrievals. The size of viewing pixels is different between the retrievals. In comparison with model and assimilation results, both retrievals are gridded to same resolution (2.5° × 2.5°), using weighting factors for the surface overlap between satellite pixel and grid cell. As a result, the viewing pixel size difference will not affect the comparison results too much.

2.1.3 INTEX-B aircraft data

The in situ vertical profile data were obtained using the UC Berkeley Laser-Induced Fluorescence (TD-LIF) instrument on DC-8 during the Intercontinental Chemical Transport Experiment Phase B (INTEX-B) campaign over the Gulf of Mexico (Singh et al., 2009). Thornton et al. (2003) and Bucsela et al. (2008) provide a detailed description and discuss the performance of the measurement. In the comparison between model and assimilation results, the data were binned on a pressure grid, with an interval of 30 hPa, whereas the model output was interpolated to the time and space of each sample. The standard deviation of variability within a grid cell is considered to represent the uncertainty. Data collected over highly polluted areas (over Mexico City and Houston) have been removed from the comparison, since it can cause a serious representativeness error in the comparison (i.e., the model resolution is too coarse). The comparisons were made for morning (8–10 a.m.) and afternoon (2–4 p.m.) conditions in March 2006.

Global NO_x emissions

K. Miyazaki et al.

Title Page

Abstract

Introduction

Conclusions

References

Tables

Figures

◀

▶

◀

▶

Back

Close

Full Screen / Esc

Printer-friendly Version

Interactive Discussion



2.1.4 DANDELIONS lidar data

The Netherlands National Institute for Public Health and the Environment (RIVM) NO₂ lidar uses the Differential Absorption Lidar (DIAL) technique to observe vertical NO₂ profiles. Volten et al. (2009) provides a detailed description of the measurement during the Dutch Aerosol and Nitrogen Dioxide Experiments for Validation of OMI and SCIAMACHY (DANDELIONS) campaign. In comparison with the lidar data, the model output was interpolated to each sampling level of the lidar at Cabauw. The results were binned on a height grid, with an interval of 100 m. Lidar profiles have a spatial representatively of 2 km in viewing direction and approximately 12 km in the direction of the wind. The model resolution is much coarser and thus the observation has a large representativeness error. The model grid points used for the interpolation around Cabauw are located at Belgium, Northern-Eastern Netherlands, Western Germany, and on the North Sea. Boundary layer conditions are very different among the grid points especially between land and ocean. To avoid a possible large representativeness error in particular under the developed boundary layer condition, the profiles obtained only before 12 p.m. were used for the comparison.

2.2 A global chemical transport model CHASER

A global CTM for the troposphere, CHASER, developed by Sudo et al. (2002b), is used as a forecast model in the data assimilation system. CHASER includes detailed chemical and transport processes in the troposphere, including 88 chemical and 25 photolytic reactions with 47 chemical species. CHASER is coupled to the atmospheric general circulation model, Center for Climate System Research/National Institute for Environmental Studies/Frontier Research Center for Global Change (CCSR/NIES/FRCGC) atmospheric general circulation model (AGCM) ver. 5.7b, on a horizontal resolution of T42 (2.8°) and 32 vertical levels from the surface to 4 hPa. Metrological fields are provided by the AGCM at every time step of CHASER (i.e., every 20 min), in which the AGCM fields are nudged toward National Centers for Environmental

Title Page

Abstract

Introduction

Conclusions

References

Tables

Figures

◀

▶

◀

▶

Back

Close

Full Screen / Esc

Printer-friendly Version

Interactive Discussion



**Global NO_x
emissions**

K. Miyazaki et al.

[Title Page](#)[Abstract](#)[Introduction](#)[Conclusions](#)[References](#)[Tables](#)[Figures](#)[◀](#)[▶](#)[◀](#)[▶](#)[Back](#)[Close](#)[Full Screen / Esc](#)[Printer-friendly Version](#)[Interactive Discussion](#)

Prediction/Department of Energy Atmospheric Model Intercomparison Project II (GPS-NCEP/DOE AMIP-II) reanalysis (Kanamitsu et al., 2002) at every time step of the AGCM to reproduce past meteorological conditions. The transport processes include sub grid-scale (parameterized) convective transport and vertical diffusion in addition to grid-scale advection. A more detailed description of the CHASER model is presented by Sudo et al. (2002b), Sudo and Akimoto (2007), and Nagashima et al. (2010). The extensive evaluation of the overall CHASER model performance was performed by Sudo et al. (2002a). The relative performance of the CHASER NO₂ simulation in comparison to other CTMs is evaluated by Van Noije et al. (2006).

The anthropogenic emissions of NO_x are based on an inventory of national emissions obtained from the Emission Database for Global Atmospheric Research (EDGAR) version 3.2 for the year 1995 and 2000 (Olivier et al., 2005), which are reported as yearly mean. Emissions from biomass burning are determined on a monthly basis according to the satellite-derived carbon emission estimates from the Global Fire Emissions Data base (GFED) version 2.1 (Randerson et al., 2007). NO_x emissions from soils are based on Global Emissions Inventory Activity (GEIA) (Graedel et al., 1993), which are reported as monthly mean. NO_x emissions over Asia were obtained from Regional Emission inventory in Asia (REAS) version 1.1 (Ohara et al., 2007) for the year 1995 and 2000. The emissions for the simulation years 2005–2006 are obtained by extrapolating the emission inventories from the years 1995 and 2000. Total amounts of these surface NO_x emissions for January, April, July, and October in 2005 are 42.9, 37.6, 46.3, and 39.2 Tg N yr⁻¹, respectively. The monthly/yearly emission data were linearly interpolated at each time step of the CHASER and used in the simulation. The total lightning NO_x production is globally scaled to 7.5 Tg N yr⁻¹, and its distribution is calculated at each time step of CHASER using the convection scheme in the AGCM and the parameterization of Price and Rind (1992). The total aircraft NO_x emission is 0.55 Tg N yr⁻¹, which is obtained from the EDGAR inventory.

We apply a diurnal variability scheme to the emissions depending on the dominant category for each area: anthropogenic, biogenic, and soil emissions. Note that

Global NO_x emissions

K. Miyazaki et al.

Title Page

Abstract

Introduction

Conclusions

References

Tables

Figures

◀

▶

◀

▶

Back

Close

Full Screen / Esc

Printer-friendly Version

Interactive Discussion



a diurnal scaling of each emission category separately is a more logical approach. However, this approach cannot be applied in this study since only the total emission is processed in the model simulation. Van der A et al. (2008) determined the dominant source categories for each area based on the analysis of the seasonality of observed tropospheric NO₂ column. Following the result of Van der A et al. (2008) and the setting of Boersma et al. (2008), we apply anthropogenic-type diurnal variations (with maxima in morning and in evening with a factor of about 1.4) in Europe, Eastern China, Japan, and North America; biomass burning-type variations (with a rapid increase in morning and maxima emissions in the mid-day with a maximum factor of about 3) in Central Africa and South America; and soil-type diurnal variations (with maxima emissions in afternoon with a factor of about 1.2) in the grasslands or sparsely vegetated areas of Australia, Sahara, and Western China. The soil NO_x emission dependence on temperature and moisture (Yienger and Levy, 1999) is not explicitly considered. The total amount of emissions does not change by applying the diurnal variability scheme.

2.3 Data assimilation

Data assimilation is a technique to combine observational information with a model. We employ an ensemble Kalman filter approach to estimate NO_x emissions from NO₂ data. The assimilation runs were performed for six individual months (starting from 1st to 30th of each month), January, April, July, and October in 2005, and March and September in 2006. The initial conditions for meteorological and chemical fields were obtained from long-term (about a year) simulation of the CHASER for each month. The results for 2005 are used to investigate the seasonal variability of the emission, while those for 2006 are used to validate the assimilation results against in situ observations.

2.3.1 Ensemble Kalman filter

The data assimilation technique employed is a local ensemble transform Kalman filter (LETKF). LETKF is related to the ensemble square root filter (SRF) method (e.g.,

Global NO_x
emissions

K. Miyazaki et al.

Title Page

Abstract

Introduction

Conclusions

References

Tables

Figures

◀

▶

◀

▶

Back

Close

Full Screen / Esc

Printer-friendly Version

Interactive Discussion



Whitaker and Hamill 2002) which generates an analysis ensemble mean and covariance which satisfy the Kalman filter equations for linear models (e.g., Ott et al., 2004). The LETKF has conceptual and computational advantages over the original EnKF (e.g., Ott et al., 2004; Hunt et al., 2007). The LETKF performs the analysis locally in space and time, reducing sampling errors caused by limited ensemble size. It also reduces the computational cost by performing most calculations in parallel (e.g., Miyoshi and Yamane, 2007).

Here we briefly introduce the LETKF technique following Hunt et al. (2007) and Kalnay (2010). The LETKF updates the analysis and transforms a background ensemble ($\mathbf{x}_i^b; i = 1, \dots, k$) into an analysis ensemble ($\mathbf{x}_i^a; i = 1, \dots, k$), where \mathbf{x} represents the model variable; \mathbf{b} the background state; \mathbf{a} the analysis state; and k the ensemble size. In the forecast step, a background ensemble, \mathbf{x}_i^b , is globally obtained from the evolution of each ensemble member using the forecast model. The background ensemble mean, $\overline{\mathbf{x}^b}$, and its perturbations (spread), \mathbf{X}^b , are estimated from the ensemble forecast,

$$\overline{\mathbf{x}^b} = \frac{1}{k} \sum_{i=1}^k \mathbf{x}_i^b; \quad \mathbf{X}^b = \mathbf{x}_i^b - \overline{\mathbf{x}^b}. \quad (1)$$

These are $N \times k$ matrices, where N indicates the system dimension and k indicates the ensemble size. The background error covariance follows from the assumption that background ensemble perturbations \mathbf{X}^b sample the forecast errors,

$$\mathbf{P}^b = \mathbf{X}^b (\mathbf{X}^b)^T. \quad (2)$$

In the analysis step, an ensemble of background vectors, \mathbf{y}_i^b , and an ensemble of background perturbations in the observation space, \mathbf{Y}^b , are obtained as follows:

$$\mathbf{y}_i^b = H(\mathbf{x}_i^b); \quad \mathbf{Y}^b = \mathbf{y}_i^b - \overline{\mathbf{y}^b}, \quad (3)$$

where H is the non-linear observational operator that converts an N -dimensional state vector to a p - (number of observation) dimensional observational vector. To compute

the analysis for each grid point independently, the local analysis error covariance is estimated in the ensemble space:

$$\tilde{\mathbf{P}}^a = \left[(k-1)/\Delta + (\mathbf{Y}^b)^T \mathbf{R}^{-1} \mathbf{Y}^b \right]^{-1}, \quad (4)$$

where \mathbf{R} denotes the $p \times p$ observation error covariance. To prevent an underestimation of background error covariance and resultant filter divergence (e.g., Houtekamer and Mitchell, 1998) caused by model errors and sampling errors, the covariance inflation technique (with a covariance inflation parameter, Δ , in Eq. 4) is applied to inflate the forecast error covariance at each analysis step (see also Sect. 2.3.2).

Using $\tilde{\mathbf{P}}^a$, the transformation matrix, \mathbf{T} , is given by,

$$\mathbf{T} = [(k-1)\tilde{\mathbf{P}}^a]^{1/2} \quad (5)$$

\mathbf{T} is a $k \times k$ matrix which analyzes the variables for each grid point (Hunt et al., 2007). The dimension k is generally smaller than N , and calculations of large vectors or matrices with N dimension are not necessary to obtain the \mathbf{T} matrix. Then, we can update the ensemble mean by

$$\bar{\mathbf{x}}^a = \bar{\mathbf{x}}^b + \mathbf{X}^b \tilde{\mathbf{P}}^a (\mathbf{Y}^b)^T \mathbf{R}^{-1} (\mathbf{y}^o - \bar{\mathbf{y}}^b), \quad (6)$$

where \mathbf{y}^o represents the observation vector. The new analysis ensemble perturbation matrix in the model space \mathbf{X}^a is simultaneously obtained by transforming the background ensemble \mathbf{X}^b with a transform matrix \mathbf{T} at every grid point ($\mathbf{X}^a = \mathbf{X}^b \mathbf{T}$), while the new analysis ensemble in the model space, \mathbf{x}_i^a , is obtained from the combination of the background mean and ensemble perturbations ($\mathbf{x}_i^a = \bar{\mathbf{x}}^a + \mathbf{X}_i^a$).

The EnKF approaches always have a spurious long distance correlation problem because of imperfect sampling of the probability distribution due to limited ensembles (e.g., Houtekamer and Mitchell, 2001). To improve the performance of the data assimilation with reducing the ensemble size, we employ a covariance localization technique.

We assumed that observations located far from the analysis point have larger errors

Title Page

Abstract

Introduction

Conclusions

References

Tables

Figures

◀

▶

◀

▶

Back

Close

Full Screen / Esc

Printer-friendly Version

Interactive Discussion



and those observations have less impact on the analysis (e.g., Miyoshi and Yamane, 2007). As a result, the analysis is solved at every grid point by choosing nearby observations (depending on the localization length, see Sect. 4.2). The new global analysis ensemble is obtained by combining the local analyses obtained for each grid point.

5 The tropospheric AK provided in the OMI retrieval product is used in the assimilation. The use of the average kernel in the observation operator removes the contribution of the retrieval error due to the a priori profile error (Eskes and Boersma, 2003);

$$\mathbf{y}_i^b = H \left(\mathbf{x}_i^b \right) = \sum_{i=1}^k a_i \mathbf{x}_i^b, \quad (7)$$

10 where a_i is each component of the AK at i -th vertical level, and \mathbf{x}_i^b is the collocated model profile expressed in terms of NO_2 sub-columns for each of the retrieval vertical layers. Simulated NO_2 fields are in this way are converted into tropospheric NO_2 columns using the simulated the AK, the surface pressure obtained from the AGCM simulation, and the tropopause height used in the OMI retrieval product.

2.3.2 NO_x emission estimation

15 A top-down approach with a bottom-up emission inventory (as a priori) was used to obtain posterior estimates of surface NO_x emissions. To accomplish this, we applied the state augmentation method (e.g., Aksoy et al., 2006). In this method, the model parameter is estimated by including it as part of the state vector using the ensemble model simulations and observations. This approach allows indirect relationships
20 between NO_2 concentrations and NO_x emissions caused by complex chemical and transport processes (e.g., changes in the NO_2/NO_x ratio) to be considered through the use of the background error covariance produced by ensemble CTM forecasts. This advanced approach differs from methods based on the modeled local ratio between concentrations and emissions (e.g., Martin et al., 2003). In our approach, the back-
25 ground error covariance, estimated from the ensemble CTM simulations, varies with

[Title Page](#)[Abstract](#)[Introduction](#)[Conclusions](#)[References](#)[Tables](#)[Figures](#)[◀](#)[▶](#)[◀](#)[▶](#)[Back](#)[Close](#)[Full Screen / Esc](#)[Printer-friendly Version](#)[Interactive Discussion](#)

time and space depending on atmospheric conditions. Accordingly, the local analysis increment, which is the a posteriori emission minus the a priori emission, is not solely determined by the difference in the observed and simulated concentrations.

The forecast process also plays important roles in the data assimilation. It propagates observation information, inflates the analysis spread, and determines the quality of the first guess. A linearized forecast model (\mathbf{M}) provides a first guess of the state vector for data assimilation based on the background error covariance from the previous analysis time t_n to the new analysis time t_{n+1} ,

$$\mathbf{P}^b(t_{n+1}) = \mathbf{M}\mathbf{P}^a(t_n)\mathbf{M}^T + \mathbf{Q}. \quad (8)$$

In this study, because of the lack of any applicable model, a persistent forecast model ($\mathbf{M} = \mathbf{I}$) is used for the NO_x emissions. In our setting, without any treatment that prevents the parameter covariance magnitude reduction (e.g., by the forecast model error covariance term \mathbf{Q}), the analysis can no longer be influenced by the observations, because of an overestimation of the confidence in the model. To prevent covariance underestimation, the analyzed standard deviation (i.e., background error) is artificially inflated back to a minimum predefined value at each analysis step. This minimum value used in this study is chosen as 30 % of the initial standard deviation based on sensitivity experiments. The analysis spread can be very small in some cases owing to effective corrections by the data assimilation. Because of the inflation in our daily analysis, the emission analysis can capture short-term variations of NO_x emissions. This is different from some previous studies that estimated emissions based on monthly mean data (e.g., Martin et al., 2003; Wang et al., 2007; Chai et al., 2009; Kurokawa et al., 2009). A daily analysis improves upon the monthly-mean inversion by accounting for the variability in the chemical feedbacks of NO_x emissions and by reducing the dependence of the a priori emissions (Zhao and Wang, 2009). Small random noises were also added to the analysis spread as the random forecast model error after the covariance inflation at each analysis step, with a magnitude of 4 % of the initial spread.

Uncertainty information on the a priori emission is required to create the initial emission error covariance. We expect large uncertainty in the a priori emission, as a result

**Global NO_x
emissions**

K. Miyazaki et al.

[Title Page](#)[Abstract](#)[Introduction](#)[Conclusions](#)[References](#)[Tables](#)[Figures](#)[◀](#)[▶](#)[◀](#)[▶](#)[Back](#)[Close](#)[Full Screen / Esc](#)[Printer-friendly Version](#)[Interactive Discussion](#)

**Global NO_x
emissions**

K. Miyazaki et al.

[Title Page](#)[Abstract](#)[Introduction](#)[Conclusions](#)[References](#)[Tables](#)[Figures](#)[I◀](#)[▶I](#)[◀](#)[▶](#)[Back](#)[Close](#)[Full Screen / Esc](#)[Printer-friendly Version](#)[Interactive Discussion](#)

of the neglected seasonality in the anthropogenic emissions and large discrepancy between different anthropogenic (e.g., EDGAR vs. REAS) and biomass burning emission inventories (e.g., EDGAR vs. GEIA). The initial error is set to 40 % of the a priori emission. Note that the emission analysis is generally no longer sensitive to the initial error after some (e.g., several weeks) assimilation cycles. Only the combined total emission is optimized in the analysis. This is to reduce the degree of freedom in the analysis and to avoid the difficulty associated with estimating background errors for each category source separately. The uncertainty in the a posteriori emission is reduced if the analysis converges to a true state, which is represented by the analysis spread in the EnKF data assimilation. For instance, in January, the mean analysis spread becomes about 30–40 % of the initial spread after some assimilation cycles over Northern Europe, the United States North, America, Eastern China, India, and Northern Africa, demonstrating significant reductions in the emission uncertainty through the data assimilation over these areas. However, since the analysis spread is artificially inflated to the predefined constant value during the analysis step in our system, this information is not used to measure the a posteriori uncertainty. Instead, the standard deviations of the estimated daily emissions during the analysis period are used as the uncertainty information. Details analyses on the analysis spread information will be performed using more advanced inflation techniques in future studies (see also discussions in Sect. 4.2).

The surface emission factor is analyzed and updated using observations at an analysis interval of every 100 min (i.e., every orbit cycle of OMI observations). This setting is useful to reduce the time discrepancy between the observation and the model in the data assimilation. Tropospheric NO₂ shows a distinct diurnal variation, and any time discrepancy will result in serious model error. The a posteriori emissions estimated using the analyzed emission factor are used in the next step ensemble model simulations.

2.3.3 Super-observation approach

The spatial resolution of the OMI data (= 13 km × 24 km) is much finer than that of the CHASER model grid (= 2.8°). Thus, there are large representativeness errors in the model because of unresolved small-scale variations. To fill the spatial scale gaps and to produce more representative data, a super-observation approach has been developed. The spatial resolution of the super-observation was set to be 2.5°, almost equivalent to the CHASER model resolution. Note that the spatial distribution of the super-observation is constant, whereas the CHASER uses a Gaussian (variable) grid. A super-observation is generated by averaging all data located within a super-observation grid cell;

$$\bar{y} = \left(\sum_{l=1}^m w_l y_l \right) / \left(\sum_{l=1}^m w_l \right), \quad (9)$$

where \bar{y} is the super-observation concentration; y_l is the concentration of individual data; w_l is the weighting factor; m is the number of observation within a super-observation grid. The weighting factor for individual data, w_l , is estimated as the ratio of the coverage area by individual data pixels and the total coverage area (sum of the coverage area by all data used for generating a super observation) for a super-observation grid; i.e., data with high coverage are assumed to be more reliable (i.e., larger w_l). The same weighting factors are applied for averaging the AK.

The measurement error for the super-observation is computed similar to in Eskes et al. (2003),

$$\sigma_{\text{super,mean}} = \left(\left(\sum_{l=1}^m w_l \sigma_l \right) / \left(\sum_{l=1}^m w_l \right) \right) \sqrt{\frac{1-c}{m} + c}, \quad (10)$$

in which the observation error (σ_l) is averaged over a grid with the weight (w_l), and the averaged error is multiplied by the error correlation (c) among data. The error correlation determines the quality of the super-observation, as illustrated in Fig. 1a. We

Title Page

Abstract

Introduction

Conclusions

References

Tables

Figures

◀

▶

◀

▶

Back

Close

Full Screen / Esc

Printer-friendly Version

Interactive Discussion



Global NO_x
emissions

K. Miyazaki et al.

Title Page

Abstract

Introduction

Conclusions

References

Tables

Figures

◀

▶

◀

▶

Back

Close

Full Screen / Esc

Printer-friendly Version

Interactive Discussion



apply 15 % error correlation. Errors in for instance the cloud, albedo and aerosol treatment in the NO₂ retrieval are typically correlated in space, but a quantitative number for this correlation is difficult to estimate. The super-observation measurement error also decreases as the number of observations used for the super-observation increases.

A typical number of OMI observations used for a super-observation is about 120–250, resulting in about 60 % reduction of the mean measurement error.

The representativeness error is also considered if the super-observation grid is not fully covered by OMI pixels. A representativeness error as a function of the OMI coverage was estimated based on grid cells which were well-covered by OMI pixels (i.e., more than 90 % coverage, excluding remote areas where the mean concentration is less than $0.5 \times 10^{15} \text{ mol cm}^{-2}$). For these well-covered cells, we artificially decreased the coverage by randomly reducing the number of observations used for constructing a super-observation. Then, a representativeness error factor (f_{rep}) is estimated based on the relationships between the coverage area ($\alpha = 0 \sim 1$) and the super-observation concentration as follow;

$$f_{\text{rep}}(\alpha) = \left| \left(\frac{1}{m} \sum_{l=1}^m y_l - \frac{1}{\alpha \times m} \sum_{l=1}^{\alpha \times m} y_l \right) / \left(\frac{1}{m} \sum_{l=1}^m y_l \right) \right|. \quad (11)$$

For coarse grid cells completely covered by OMI observation footprints ($\alpha = 1$), this representativeness error is zero. For cells covered by just one OMI pixel the representativity error approaches the variability of individual measurements around the grid cell mean. The mean representativeness error factor averaged over the globe and over a month almost linearly increases as the coverage decreases, with a steeper increase for coverage area less than 10 % (Fig. 1b). The mean averaged function is applied to estimate the representativeness error of each super-observation according to its coverage areas (α):

$$\sigma_{\text{super,rep}} = f_{\text{rep}}(\alpha) \times \bar{y} \quad (12)$$

where the area dependence of the representativeness error function was neglected.

Finally, the total super-observation error is computed as a combination of the measurement error and the representativeness error, $\sqrt{\sigma_{\text{super,mean}}^2 + \sigma_{\text{super,rep}}^2}$.

3 Simulated and retrieved tropospheric NO₂ columns

Here we investigate the performance of the model and satellite retrievals. The AK has been applied to the CHASER profiles to compare with satellite retrievals precisely. The CHASER concentrations are interpolated to the retrieval pixels at the local overpass time of the satellite, and then both the retrieved and simulated concentrations are mapped onto a same horizontal resolution of $2.5^\circ \times 2.5^\circ$.

3.1 Global distribution

Figure 2 compares global distributions of annual-mean tropospheric NO₂ columns obtained from the OMI retrievals, the SCIAMACHY retrieval, and the CHASER simulation at the local overpass time of the retrievals (10:00 and 13:30, respectively). The retrievals and the model show very similar spatial distributions. Large-scale pollution with high concentrations is observed over Eastern China, Europe, and the Eastern United States. High concentrations are also found over the Highveld region of Southern Africa, Central Africa, Japan, South Korea, India, Southeast Asia, and other mega cities. Low concentrations, mostly smaller than the OMI noise level, are observed over the oceans and remote regions. Note that the annual-mean distribution in both the model and retrievals may be positively biased compared to the true annual-mean local time NO₂ concentration. This occurs especially over tropical regions, since the sampling under clear sky condition occurs in relatively fewer observations during the wet seasons than during the dry seasons (Van Noije et al., 2006).

The OMI retrievals agree well with the SCIAMACHY retrieval, with a global spatial correlation of 0.90–0.93, a global mean root-mean-square error (RMSE) of about $0.35\text{--}0.66 \times 10^{15} \text{ mol cm}^{-2}$, and the global mean bias (OMI minus SCIAMACHY) of -0.02--

[Title Page](#)[Abstract](#)[Introduction](#)[Conclusions](#)[References](#)[Tables](#)[Figures](#)[◀](#)[▶](#)[◀](#)[▶](#)[Back](#)[Close](#)[Full Screen / Esc](#)[Printer-friendly Version](#)[Interactive Discussion](#)

**Global NO_x
emissions**

K. Miyazaki et al.

Title Page

Abstract

Introduction

Conclusions

References

Tables

Figures

◀

▶

◀

▶

Back

Close

Full Screen / Esc

Printer-friendly Version

Interactive Discussion



$0.12 \times 10^{15} \text{ mol cm}^{-2}$ for the monthly mean concentration. The OMI mean difference compared to the SCIAMACHY is mostly positive and is larger for DOMINO v1 than DOMINO v2, whereas the RMSE compared to the SCIAMACHY retrieval is higher for DOMINO v2 than DOMINO v1. Higher concentrations are observed in DOMINO v1 than in DOMINO v2 over Northern Europe, the Northern-Eastern United States, and Eastern China, with a mean difference of about 10–30 % (Fig. 2). Apart from the global mean, the SCIAMACHY retrieval shows higher NO₂ concentrations than the OMI retrievals over urban areas around megacities and lower concentrations over biomass burning regions (Boersma et al., 2008), probably mainly as a result of the difference in observation time, as will be further discussed in Sect. 3.3.

Although the CHASER reproduces well the general features of the observed NO₂ patterns (with a global spatial correlation of 0.71–0.89 depending on season and retrieval), similar to that estimated using other global CTMs (Van Noije et al., 2006; Huijnen et al., 2010), systematic differences exist between the model and retrievals (Table 1). The model is generally negatively biased relative to the OMI retrievals, but is positively biased relative to the SCIAMACHY retrieval (except in January) in the global mean. This may be partly due to the bias observed between the SCIAMACHY and OMI, dominated by the background concentrations smaller than the detection limit of OMI and the stratospheric contribution to the column. The model generally underestimates tropospheric NO₂ columns in industrial areas (Fig. 2); e.g., over Eastern China, the Eastern United States, Southwestern Europe, and Southern Africa, suggesting that anthropogenic emissions in the emission inventories are underestimated. As an exception, the model largely overestimates NO₂ columns over Northern Europe, particularly when compared to DOMINO v2. The model negative bias is also observed over biomass burning areas; e.g., over Central Africa and South America. In contrast, significant positive model biases exist in remote areas especially when compared to the SCIAMACHY data. The RMSE is largest in January in all cases.

By applying the AK, the model generally shows better agreements with satellite retrievals, as commonly found using other CTMs (Van Noije et al., 2006; Huijnen et al.,

2010). The application of the AK increased the global spatial correlation by 0.02–0.13, decreased the global mean bias by 0.01–0.32 (up to about 90 %), with larger impacts on the comparison with the SCIAMACHY retrieval than that with the OMI retrievals. The larger impacts with the SCIAMACHY AK may be attributed to larger differences between the a priori used in the SCIAMACHY retrieval and the CHASER profiles. The impact was significant over Europe and Eastern Asia and was different among seasons. For instance, the application of DOMINO v1 AK leads to a change of NO₂ column up to $-1.1 \times 10^{15} \text{ mol cm}^{-2}$ ($+1.5 \times 10^{15} \text{ mol cm}^{-2}$) over Europe in January (July). The increase (decrease) implies a larger (smaller) decrease of NO₂ concentration with height in the a priori profile used in the retrieval than in the profile simulated by the CHASER. For the OMI comparisons, the impact of the AK was weaker in the case of the DOMINO v2 than the DOMINO v1 over polluted areas, suggesting that the CHASER profile is more similar to the a priori profile used in DOMINO v2 than that in DOMINO v1.

3.2 Seasonal variation

Figure 3 compares the seasonal variations of the regional mean tropospheric NO₂ columns for major polluted and biomass burning areas. The seasonal variations are very similar among the satellite retrievals, except for clear differences between DOMINO v1 and v2 over Europe, the Eastern United States, and Southern Africa during winter. In industrial regions, the tropospheric NO₂ column is higher in winter than in summer. Biomass burning occurs especially during the dry season, in the winter and early spring, leading to a maximum concentration in these seasons over the Central Africa, Southeast Asia, and South America. These variations can be explained by the seasonal variation of surface NO_x emissions, lightning NO_x productions, the NO/NO₂ ratio, and the NO₂ lifetime. Velders et al. (2001) and Lamsal et al. (2010) investigated that the seasonal variation of NO_x lifetime, with a maximum in winter and a minimum in summer, mainly determines the seasonality of the tropospheric NO₂ columns over polluted areas. The lifetime variation reflects gas-phase oxidation of NO₂ with OH in summer with an increasing role for heterogeneous chemistry in winter (Lamsal et al.,

Title Page

Abstract

Introduction

Conclusions

References

Tables

Figures

◀

▶

◀

▶

Back

Close

Full Screen / Esc

Printer-friendly Version

Interactive Discussion



2010).

The simulated regional mean tropospheric NO₂ columns are generally lower than the observed ones in most polluted regions throughout the year. The underestimation is more obvious in winter than in other seasons over Eastern China, Europe, the Eastern United States and Southern Africa. A most obvious difference is seen over Eastern China and Southern Africa with a factor of up to 3. The timing of the seasonal variation is well represented, but the amplitude is largely underestimated by the model over these regions. Over Central Africa, South America, and Southeast Asia, biomass burning dominates the seasonal variations of NO₂ concentrations, where the maximum and minimum concentration occurs almost in the same months in the model and retrievals, but with a mean negative bias of about 20–40 % in the model.

3.3 Diurnal variation

The summertime tropospheric NO₂ columns are lower in the OMI retrieval (except for DOMINO v1 likely due to its positive bias) than in the SCIAMACHY retrieval over polluted areas, but are higher over biomass burning regions, as depicted in Fig. 4. This is mainly due to a difference in their overpass time. The afternoon lower concentration in urban areas is attributed to diurnal variations of NO₂ loss due to reaction with OH and of photolysis rates, whereas the higher concentration over biomass burning region are related to the mid-day maximum in biomass burning emissions.

To improve the simulation, we applied pre-defined functions for the diurnal variations of surface NO_x emissions (cf., Sect. 2.2). By applying the diurnal variability scheme, the CHASER shows better agreements with the satellite retrievals, with a global mean RMSE reduction of about 10–15 (30–40) % compared to the OMI (SCIAMACHY) retrievals, as similarly demonstrated using other CTMs (Van Noije et al., 2006; Boersma et al., 2008). The diurnal variability scheme generally decreases the NO₂ concentration in morning, but increases it in afternoon in the industry and biomass burning areas. Since the diurnal variation of NO_x emissions strongly influences the model-observation difference, the implementation of a realistic diurnal scheme is important to

Global NO_x emissions

K. Miyazaki et al.

Title Page

Abstract

Introduction

Conclusions

References

Tables

Figures

◀

▶

◀

▶

Back

Close

Full Screen / Esc

Printer-friendly Version

Interactive Discussion



obtain reasonable emissions. The impact of the diurnal scheme on surface emission estimations will be further discussed in Sect. 6.

4 Optimizing the data assimilation system

4.1 Impact of super-observation

5 By using the super-observations instead of the normal observations, the data assimilation reveals a better agreement with the assimilated DOMINO v2 data. An increasing spatial correlation of 0.03–0.05 and a decreasing global mean RMSE of 30–40 % were observed in an experiment with the super-observations compared to normal observations. Improvements by the super-observation approach were commonly observed at
10 both a resolution of the super-observations (i.e., 2.5°) and at finer scale (i.e., 1°). In the case with the normal observations, observation data contains large representativeness error especially in polluted areas, which may prevent the analysis from efficiently and stably reducing the systematic errors of the model (i.e., analysis increments were sometime very noisy and large). The super-observation approach provides more representative data and helps to obtain systematic analysis increments, although the error
15 correlation assumed in making the super-observation is uncertain. Furthermore, the super-observation approach reduces the computational cost of the data assimilation, by reducing the number of data processed in the analysis step.

4.2 Sensitivity to assimilation parameters

20 Various factors affect the performance and the computational cost of the data assimilation. We have conducted sensitivity experiments to obtain an optimal setting for the data assimilation, as summarized in Table 2. First, the analysis is sensitive to the localization length. The lifetime of NO_x in the lower troposphere varies from several hours to a day, with a longer lifetime during winter than during summer. In addition,

Global NO_x
emissions

K. Miyazaki et al.

Title Page

Abstract

Introduction

Conclusions

References

Tables

Figures

◀

▶

◀

▶

Back

Close

Full Screen / Esc

Printer-friendly Version

Interactive Discussion



long-range transport of, for instance, peroxyacetyl nitrate (PAN) can propagate local NO_x source information to remote places. As a result, the NO_x emission and NO₂ concentration will have long distance correlations in some cases. Remote observation will not affect the analysis if the localization length is short, while the analysis will suffer from serious sampling errors by using a too long localization length in combination with a small ensemble size. The optimal localization length was found to be 450 km for the global analysis in January. The optimal length may depend on the location and season because of changes in the NO₂ lifetime and wind patters. Second, a large ensemble size is essential to capture background error covariance structures properly, but also increases the computational cost. The analysis improved by increasing the ensemble size to 32, whereas it did not vary significantly by increasing it further. Thus, ensemble size of (or greater than) 32 was preferred to remove sampling errors. Finally, the use of the covariance inflation (cf., Eq. 4) slightly improved the analysis together with the conditional covariance inflation (cf., Sect. 2.3.2), since it reduces the underestimation in the background error covariance. Although there is no clear optimal value, we employ 5% covariance inflation.

The performance of the tropospheric NO₂ column data assimilation with the optimized settings was evaluated from the chi-square (χ^2) test (e.g., Ménard and Chang, 2000; Zupanski and Zupanski, 2006). The χ^2 is estimated from the ratio of the actual observation-minus-forecast (OmF) to the estimated background covariance. For this test, the innovation statistics are diagnosed from the OmF ($\mathbf{y}^o - H(\mathbf{x}^b)$), the estimated error covariance in the observational space ($\mathbf{H}\mathbf{P}^b\mathbf{H}^T + \mathbf{R}$), and the number of observations, m .

$$\mathbf{Y} = \frac{1}{\sqrt{m}}(\mathbf{H}\mathbf{P}^b\mathbf{H}^T + \mathbf{R})^{-1/2}(\mathbf{y}^o - H(\mathbf{x}^b)). \quad (13)$$

Using this statistics, the χ^2 is defined as follow:

$$\chi^2 = \text{trace } \mathbf{Y}\mathbf{Y}^T, \quad (14)$$

where H is the non-linear observational operator and the \mathbf{H} is the linearization of the observation operator. The mean values of the χ^2 indicate that optimized system is generally within 30 % difference from the ideal value of 1 (Fig. 5). The mean positive bias of the χ^2 is reduced through data assimilation cycles, indicating that the data assimilation tends to provide the optimal solution. The remaining mean positive bias of the χ^2 value ($\sim 25\%$) indicates an persistent underestimation of the forecast error variance. The magnitude of the underestimation varied largely with time and space. Although the conditional covariance inflation to the emissions acted to amplify the forecast spread of the tropospheric NO_2 column, the adaptive covariance inflation technique (e.g., Anderson, 2009) may help to more properly introduce the inflation to the emissions.

5 Data assimilation results

5.1 Analyzed NO_x emissions

The surface NO_x emissions obtained from the assimilation of DOMINO v2 data for four months in different seasons are shown in Figs. 6 and 7, and summarized in Table 3. The monthly mean optimized NO_x global source is up to 12 % higher than the a priori emission. Regional differences are more obvious, with a factor of up to about 2.5. The analysis increment is generally positive over Eastern China, North America, Australia, Northern India, and Southern Africa. An obvious increment is observed over Eastern China, with a factor of up to about 1.7 at regional scale with maxima in January and July, implying that REAS 1.1 (the a priori) largely underestimates the NO_x emissions over Eastern China in 2005, as commonly revealed by Van Noije et al. (2006) and Kurokawa et al. (2009), but for different years. Part of this underestimation may be attributed to the assumed linear trend in the a priori emissions calculated based on variations between 1995 and 2000. The assumed trend may cause an underestimation of the changes in the period 2000–2005 (cf., Sect. 2.2). As shown in Fig. 7, the bottom-up emissions obtained from the latest inventories (EDGAR ver. 4.1, GFED ver. 3.1, and

[Title Page](#)[Abstract](#)[Introduction](#)[Conclusions](#)[References](#)[Tables](#)[Figures](#)[◀](#)[▶](#)[◀](#)[▶](#)[Back](#)[Close](#)[Full Screen / Esc](#)[Printer-friendly Version](#)[Interactive Discussion](#)

GEIA) are larger than the a priori emissions (REAS 1.1) and are close to the a posteriori emissions over Eastern China. However, the wintertime and summertime maxima of the NO_x emissions are not reproduced by both the a priori or the latest inventories. The analysis increment also shows significant spatial variations within the regional domains. The estimated emissions are higher than the a priori emissions around large cities in Eastern Asia, such as Beijing, Tianjin, Nanjing, Hong Kong, Seoul, and Osaka, whereas it is lower in most remote areas (upper panels in Fig. 8). Consequently, differences in NO_x emissions between large cities and underdeveloped areas generally become larger for the a posteriori emissions than the a priori emissions in Eastern Asia.

The emission inventories, both the a priori and latest ones, are significantly lower than the estimated emissions over the Eastern United States, except during summer. Within the regional domain (lower middle panels in Fig. 8), the annual mean a posteriori emissions show higher values than the a priori emissions around large cities in the Eastern United States; e.g., around Chicago, Indianapolis, Atlanta, and Florida peninsula. In contrast, the a posteriori emissions are smaller in the northern part of North America (e.g., around Montreal and Toronto), as well as around Houston, with factors of less than 0.6 being observed. A large increase in NO_x emissions also appears in the Highveld region of Southern Africa, with a factor of about 1.7 except in October.

Different from other industrial areas, the a posteriori emissions are lower than the a priori emissions over Europe, except during summer, and the latest inventories are lower than both the a priori and the a posteriori emissions. The analysis increment is very different among grid points over Europe (upper middle panels in Fig. 8). The increment is mostly positive over Northwestern Europe, including Germany, France, Switzerland, and Southern England, whereas it is negative over Southwestern and Eastern Europe. It should be noted that the extrapolation we applied to derive 2005 emissions from the 1995 and 2000 inventories may give spurious results for certain regions. For instance, the a priori emissions in Spain are unrealistically high, and are strongly decreased by the assimilation. These high emissions in Spain also contributed

**Global NO_x
emissions**

K. Miyazaki et al.

Title Page

Abstract

Introduction

Conclusions

References

Tables

Figures

◀

▶

◀

▶

Back

Close

Full Screen / Esc

Printer-friendly Version

Interactive Discussion



significantly to the European mean, which explains in part the relatively high values of the a priori emissions (the black curve in Fig. 7).

The seasonal variations in biomass burning emissions may vary greatly with year, while the data assimilation corrects the timing and the strength of emissions from biomass burning for the analysis year. Over Central Africa, the a posteriori emissions are larger than the a priori emissions in April (with a factor of 2), and smaller in July (with a factor of 0.85), reflecting observed seasonal variations in biomass burning activity (e.g., Fig. 3). As a result, the seasonal amplitude of the Central African emissions in 2005 becomes smaller in the a posteriori than the a priori emissions. Over Northern Africa, the data assimilation decreases the emissions in January with a factor of 0.7, but increases the emissions in July with a factor of 1.4. Although the annual mean a priori and a posteriori emissions values are similar over Northern Africa, the spatial distribution is largely modified by the assimilation. The assimilation decreases the emissions in the eastern part of the Northern Africa, but increases the emissions in the western part of Northern Africa (lower panels in Fig. 8). Over Southeast Asia, the data assimilation greatly increases NO_x emissions, with a largest (a factor of 2.5) increase in April. Over South America, a large increase occurs in October (a factor of 2), reflecting the high concentration observed over the Amazon (monthly mean concentration of greater than $2 \times 10^{15} \text{ mol cm}^{-2}$), which is probably a result of forest fires and was not reproduced by the a priori emission. Accordingly, the estimated emissions over Southeast Asia and South America have a maximum value in spring, while the maximum a priori emissions occur during winter (Fig. 7). The data assimilation may also capture signals related to soil emissions, for which the inventories may have large uncertainties. For example, the regional mean emissions over Australia are increased by a factor of 1.2–1.4 with a maximum increase in October. The emissions are also increased over Central China (Fig. 6). These positive increments may indicate the underestimation of soil emissions in the a priori emission. However, sector-specific estimation is needed to identify the source category.

By assimilating DOMINO v2 data, NO_x emissions from ships mostly become smaller

Global NO_x emissions

K. Miyazaki et al.

Title Page

Abstract

Introduction

Conclusions

References

Tables

Figures

◀

▶

◀

▶

Back

Close

Full Screen / Esc

Printer-friendly Version

Interactive Discussion



than the a priori emissions. The negative increment may indicate an overestimation of ship emissions in the a priori. The negative increment can also be largely influenced by an underestimation of tropospheric NO₂ columns in the retrieval. Boersma et al. (2008) found that OMI generally observes lower columns with a mean bias of $0.6 \times 10^{15} \text{ mol cm}^{-2}$ over the ocean when compared to aircraft measurements during the INTEX-B campaign. Lamsal et al. (2010) also investigated whether the errors in stratospheric NO₂ columns could cause errors in tropospheric NO₂ column retrievals over oceans. Alternatively, the data assimilation system may have difficulties in correcting weak emissions, because of the treatment of the analysis spread (cf., Sect. 2.3.2) and large observation errors. Also, the fast chemical processing in the exhaust plume of the ship is a process that is not resolved by the CTM.

As summarized in Table 3, the data assimilation increased the annual (four-month) mean NO_x emissions by about 8 % in the Northern Hemisphere (20–90° N) and by about 50 % in the Southern Hemisphere (20–90° S). The impact on the tropical total emission is small. The estimated annual mean global NO_x emissions of $45.4 \text{ Tg N yr}^{-1}$, increased by about 9 % from the a priori, is somewhat larger than that estimated from previous studies (e.g., $42.1 \text{ Tg N yr}^{-1}$, Muller and Stavrakou, 2005; $37.8 \text{ Tg N yr}^{-1}$, Martin et al., 2003; $40.3 \text{ Tg N yr}^{-1}$, Jaeglé et al., 2005). Differences in analysis years, together with those in retrieval data and models used in the analysis, may primarily contribute to the difference in NO_x emission estimates, as similarly discussed in Jaeglé et al. (2005), and as will be further discussed in Sect. 6.

5.2 Validation with satellite data

As illustrated in Fig. 9 and summarized in Table 4, the assimilation run shows a better agreement with the satellite retrieval than the model simulation for most areas. When compared with the OMI data, the spatial correlation of the global NO₂ distribution becomes 0.04–0.19 higher, and the global mean RMSE is decreased by 25–40 % by the data assimilation. The improvement is commonly observed even when compared with independent SCIAMACHY data, with an increase in the global spatial correlation of

Global NO_x emissions

K. Miyazaki et al.

[Title Page](#)[Abstract](#)[Introduction](#)[Conclusions](#)[References](#)[Tables](#)[Figures](#)[◀](#)[▶](#)[◀](#)[▶](#)[Back](#)[Close](#)[Full Screen / Esc](#)[Printer-friendly Version](#)[Interactive Discussion](#)

**Global NO_x
emissions**

K. Miyazaki et al.

[Title Page](#)[Abstract](#)[Introduction](#)[Conclusions](#)[References](#)[Tables](#)[Figures](#)[◀](#)[▶](#)[◀](#)[▶](#)[Back](#)[Close](#)[Full Screen / Esc](#)[Printer-friendly Version](#)[Interactive Discussion](#)

about 0.03–0.10 and a decrease in the global mean RMSE of about 10–25%. As an exception, the global mean bias compared to the SCIAMACHY is not improved by the data assimilation, probably because of the systematic bias between the SCIAMACHY and the assimilated data (DOMINO v2, cf., Sect. 3.1); that is, the mean concentration over land is smaller in the DOMINO v2 data than in the SCIAMACHY retrieval.

The regional mean tropospheric NO₂ columns are compared in Table 5. The negative bias of the model is largely reduced over most industrial areas by the data assimilation, especially over Eastern China, Europe, Southern Africa, and the Eastern United States. For example, the data assimilation removes the negative bias when compared to the OMI (SCIAMACHY) retrieval by about 80–90 (60–80)% over Eastern China. The negative bias is also largely removed over the Eastern United States. The persistent negative bias over Australia and Southern Africa is also largely reduced by about 10–50%. Over Europe, the data assimilation reveals large reductions in the positive bias in January, but the reduction of the negative bias in April and October is not sufficient (see below). Improvements are also observed over biomass burning areas. Obvious negative biases of the model over South America in spring and over Southeast Asia in spring-autumn are mostly (more than 65%) removed by the data assimilation. These improvements are commonly observed even when compared with the independent SCIAMACHY data.

Because of the effective corrections in NO_x emissions by the data assimilation, the OmF distributions of the tropospheric NO₂ columns narrows, and its mean value (i.e., bias) becomes smaller (Fig. 10). For instance, the standard deviations of the OmF and the mean bias become about 30% and 90%, respectively, smaller by the data assimilation over Europe. Also, a large improvement over Eastern China is related to the reduction of the negative model bias, or OmF values larger than $5 \times 10^{15} \text{ mol cm}^{-2}$. Note that since only the NO_x emissions are updated during the data assimilation, the observation-minus-analysis (OmA) is equivalent to the OmF in our system.

Although the persistent model bias is largely removed by the emission correction, there are still large disagreements between the simulated and observed NO₂ columns

**Global NO_x
emissions**

K. Miyazaki et al.

[Title Page](#)[Abstract](#)[Introduction](#)[Conclusions](#)[References](#)[Tables](#)[Figures](#)[◀](#)[▶](#)[◀](#)[▶](#)[Back](#)[Close](#)[Full Screen / Esc](#)[Printer-friendly Version](#)[Interactive Discussion](#)

in some areas. The quality and the abundance of the OMI retrieval vary largely with season and area, reflecting observation conditions (e.g., clouds, aerosols, and surface albedo), as summarized in Table 6. The observation does not effectively correct the model state when the observation error is large compared to the background error.

Insufficient improvements by the data assimilation can be attributed to a large observation error and small amounts of observations for some regions. This occurs over Europe in April and October (large errors), over the Eastern United States in January (small numbers), over South America in January and April (large errors and small numbers), over Northern Africa in April (large errors), and over Southern Africa in January (small numbers). In addition, the data assimilation run was conducted from the beginning of each month (for a month) starting from the a priori emission. A continuous run over a few months may further improve the analysis by accumulating observational information with time, although the computational cost becomes high. The agreement between the simulated and observed NO₂ fields may be further improved by a more realistic diurnal variability scheme especially over biomass burning regions (e.g., over Central Africa; cf., Sects. 3.3 and 6).

Unlike the mean bias reduction, the data assimilation did not improve the temporal correlation significantly (figure not shown). The data assimilation accumulates observational information with time and gradually changes the emissions reflecting the OmF, the background spread, and the observation error. To reproduce rapid changes in concentrations, more constraints from observations and larger inflation to the background spread (cf., Sect. 2.3.2) are required. Meanwhile, the analysis increments are also sensitive to the error correlation assumed in the super observation (e.g., Sect. 2.3.3).

5.3 Validation with profile data

Figure 11 shows a comparison of the vertical profiles of the model simulation, the data assimilation analysis, and the aircraft observations during the INTEX-B campaign. High NO₂ concentrations are observed in the boundary layer below 950 hPa in the morning (8–10 a.m.) up to 5 ppbv, and below 900 hPa in the afternoon (2–4 p.m.) up

to 0.6 ppbv. The lower concentration in the afternoon is mainly caused by chemical loss through the reaction with OH and vertical mixing in the planetary boundary layer (PBL) during day time. Both in the morning and in the afternoon, the lowest part of the profile is well reproduced by the data assimilation run, whereas the model simulation underestimates it by about 30–40 %. The assimilation of DOMINO v2 (DOMINO v1) revealed a significant increase in surface NO_x emissions with a factor of about 1.3–1.6 (1.6–1.9) around Mexico. Boersma et al. (2008) showed a similar increase in NO_x emissions in their top-down estimate using DOMINO v1 data with a factor of about 2.0 for Mexico. Above the PBL, the NO₂ concentrations decrease with height, primarily because of the NO₂/NO ratio, which decreases with temperature. Both the model and assimilation run have lower NO₂ concentrations with differences of up to 0.1 ppbv when compared to the observed value in the free troposphere. This discrepancy may be attributed to errors in the model, such as too much chemical loss of NO₂, too small lightning productions, unrealistic representations of the NO_y species partitioning, and atmospheric transport.

The comparison with lidar profiles obtained during the DANDELIONS campaign is shown in Fig. 12. Cabauw is characterized by major populated area over a few 100 km, and the model grid concentration is considered to be representative for the observation data. Both the simulated and the observed values show a rapid decrease in NO₂ concentrations within the PBL from the surface to about 600 m (Fig. 12a). The data assimilation run shows a better agreement with the observed values in the upper part of the PBL, whereas it provides concentrations that are too high near the surface. The assimilation improves the amount of NO₂ in the boundary layer, but provides concentrations that are too high near the surface. The grid cells used for the interpolation to the Cabauw tower partially cover the North Sea, and have very different boundary layer heights, which may explain the concentration gradient in the model profiles. A positive intercept near the ground surface indicates that the model has problems representing the measurement location. The near-surface concentration will be sensitive to the model resolution owing to fine-scale emission distribution and transport. The scatter

**Global NO_x
emissions**

K. Miyazaki et al.

Title Page

Abstract

Introduction

Conclusions

References

Tables

Figures

◀

▶

◀

▶

Back

Close

Full Screen / Esc

Printer-friendly Version

Interactive Discussion



plots (Fig. 12b,c) demonstrate that the data assimilation also improves the variability of the NO_2 concentration especially below 500 m. The slope is 0.46 in the case of the model simulation, whereas it is much larger (0.99) in the data assimilation run. The assimilation does not change the model profile in the free troposphere.

Changes in the NO_x fields affect the concentrations of various chemical species through chemical processes during the forecast step. The impact on ozone is analyzed for the INTEX-B campaign at Mexico City, by comparing simulated O_3 fields with vertical O_3 profiles measured from the ozone sonde. Figure 11c shows that the assimilation of OMI NO_2 data reduces the discrepancy in O_3 concentrations between the model and observation for the lower troposphere. The enhanced NO_x emissions by the data assimilation increase chemical production of O_3 . Thus, NO_x emissions updated by the data assimilation have the potential to improve the ozone chemistry in the model, although its impact on the free tropospheric ozone is not obvious in this case. These impacts will be further investigated in future studies.

6 Sensitivity to the retrieval and model setting

Independent retrievals have different qualities, vertical sensitivities, and overpass times. These differences may result in obvious changes in the emission estimates. In addition, the performance of the model plays an important role in the emission estimates because it provides the relationship between surface fluxes and atmospheric concentrations. Thus, it is important to consider the effects of these factors on the estimated emissions. Here, we investigate the sensitivity of the emission estimates to the retrieval product and model settings. The sensitivities are shown for a season when the sensitivity is largest (Fig. 13); January for the DOMINO 1 and SCIAMACHY data assimilation experiments and July for the lightning NO_x production and the diurnal variability scheme experiments, as described below.

By assimilating DOMINO v1 data instead of DOMINO v2 data, the a posteriori emissions increase by 5–45% over most areas (Fig. 13). The emission increase

[Title Page](#)[Abstract](#)[Introduction](#)[Conclusions](#)[References](#)[Tables](#)[Figures](#)[◀](#)[▶](#)[◀](#)[▶](#)[Back](#)[Close](#)[Full Screen / Esc](#)[Printer-friendly Version](#)[Interactive Discussion](#)

corresponds to higher concentrations in DOMINO v1 as compared to DOMINO v2. This difference is obvious in January over Eastern China, the Eastern United States, Europe, Northern Africa, and Southeast Asia. The comparison indicates that errors in the retrieval algorithm lead to large uncertainties in top-down emissions. The assimilation of the SCIAMACHY columns also shows significant differences especially over South America, Southern Africa, and Southeast Asia, with relative changes of about 30–80 %. The differences between the emissions estimated using the OMI and SCIAMACHY retrievals can be partly attributed to errors related to the simplified description of the diurnal variability in the model along with systematic differences between the retrievals. We note that the SCIAMACHY and DOMINO v1 products are based on a very similar algorithm, and one could expect a similar behavior for these products compared to DOMINO v2. However, Fig. 13 shows that the emission ratios are quite different in different regions. The difference may be largely attributed to the simplified diurnal variability scheme especially over biomass burning regions. In addition, the poorer spatial and temporal resolutions and less global coverage in the SCIAMACHY retrieval than in the OMI retrieval may also cause the differences.

The bias in NO_2 columns is also influenced by NO_x processes in the upper troposphere in remote areas (Napelenok et al., 2008). Boersma et al. (2005) suggested that the contribution of lightning in the middle and upper troposphere to the tropospheric NO_2 column is strongest in the tropics, with a contribution of $0.4 \times 10^{15} \text{ mol cm}^{-2}$. We found that changes in the lightning emissions have a large effect on the estimated NO_x emissions. Specifically, by reducing the global lightning productions by half (from 7.5 to 3.75 Tg N), the NO_x emissions increased by about 30–80 % over the Eastern United States, Northern Africa, and Southeast Asia in July, as similarly demonstrated by Lin et al. (2010). The performance of the mixing scheme may also affect the tropospheric NO_2 columns. A too diffusive PBL mixing may result in an underestimation of the NO_2 columns because of the reduction in the NO_2/NO ratio with height. As demonstrated in Sect. 5.3, the model used shows an underestimation in the free tropospheric NO_2 concentration during the INTEX-B campaign. This underestimation may lead to an

**Global NO_x
emissions**

K. Miyazaki et al.

Title Page

Abstract

Introduction

Conclusions

References

Tables

Figures

◀

▶

◀

▶

Back

Close

Full Screen / Esc

Printer-friendly Version

Interactive Discussion



overestimation of the estimated surface emissions in the data assimilation. Thus, realistic representations of atmospheric processes in the model are required to improve the emissions estimates. Simultaneous optimization of atmospheric (e.g., lightning) and surface NO_x sources will be performed in future studies.

5 Meanwhile, the implementation of the diurnal variability scheme largely influences the emission estimates (cf., Fig. 4). For example, the emission was decreased from the a priori by 22 % over Central Africa in the data assimilation with the diurnal variability scheme, whereas it was increased by 30 % in the data assimilation with a constant emission. Similar differences between the experiments with and without the diurnal
10 variation scheme were also found over industrial areas (e.g., over Europe). Although the estimated emission was largely affected by the diurnal variability scheme, the prescribed diurnal variation profile is highly simplified, and it will not accurately represent the temporal variations of emissions. An alternate approach is required to determine the diurnal variability profile from analyses of multiple polar or future geostationary satellite instruments.
15

7 Conclusions

We have developed an advanced data assimilation system to estimate global NO_x emissions. An ensemble Kalman filter approach was developed, in which the state augmentation method was employed to estimate daily global surface emissions of NO_x with a horizontal resolution of 2.8° using OMI tropospheric NO₂ column retrievals. This approach allows us to (1) accumulate observation information with time and (2) reflect the non-direct relationship between the emissions and tropospheric columns because of the use of the background error covariance dynamically estimated from the ensemble of CTM forecasts. A super-observation approach was employed to produce data
20 representative for a model grid cell, which helped improve the assimilation analyses.

The inversion increased the NO_x emissions in Eastern China, the Eastern United States, Southern Africa, and Central-Eastern Europe, suggesting that the

Global NO_x emissions

K. Miyazaki et al.

Title Page

Abstract

Introduction

Conclusions

References

Tables

Figures

◀

▶

◀

▶

Back

Close

Full Screen / Esc

Printer-friendly Version

Interactive Discussion



anthropogenic emissions are mostly underestimated in the a priori emissions that were constructed based on bottom-up inventories. An obvious increase in the emission was observed over Eastern China, with a factor of up to 1.7. A large increase in NO_x emissions also appears in the Highveld region of Southern Africa and over the Eastern United States, with a factor of about 1.4–2.5. Different from other industrial areas, the regional mean a posteriori emissions were lower than the a priori emissions over Europe, although the analysis increment showed obvious spatial variations (e.g., mostly positive over Northwestern Europe and negative over Eastern and Southwestern Europe). The data assimilation also corrected the timing and the amplitude of the emissions from biomass burning, with a large increase over Central Africa (with a factor of 2) and Southeast Asia (with a factor of 2.5) in April and over South America (with a factor of 2) in October. As a result, the a posteriori emissions over these biomass burning areas showed the maximum value in spring in the analysis year 2005, which differed from the wintertime maximum for the emission inventories. The estimated emissions are generally more similar to the latest inventories obtained from the EDGAR 4.1, GFED 3.1, and GEIA data sets than the a priori emissions constructed based on older inventories, although there are large discrepancies between the estimated emissions and the latest inventories over Europe, the Eastern United States, Central Africa, and Southeast Asia.

The data assimilation results were validated by comparing the simulated NO₂ concentrations with independent data: the SCIAMACHY satellite retrieval and vertical profiles obtained during the INTEX-B and DANDELIONS campaigns. The emission correction led to significant reductions in the disagreement between the simulated and observed NO₂, suggesting that the data assimilation improves the representation of surface NO_x emissions. The emission correction improved the NO₂ profiles within the boundary layer below about 500 m, whereas its impact was small in the free troposphere. Thus, more constraints on the free tropospheric processes (e.g., lightning productions) are required for further improving the vertical distribution of the NO_x sources. Meanwhile, although OMI provides global coverage of NO₂ concentrations,

**Global NO_x
emissions**

K. Miyazaki et al.

[Title Page](#)[Abstract](#)[Introduction](#)[Conclusions](#)[References](#)[Tables](#)[Figures](#)[I◀](#)[▶I](#)[◀](#)[▶](#)[Back](#)[Close](#)[Full Screen / Esc](#)[Printer-friendly Version](#)[Interactive Discussion](#)

the effectiveness of the data assimilation was largely determined by the quality and the frequency of the observation.

Because of various error sources in both the model and the satellite retrieval, there are large uncertainties in the estimated emissions. In fact, the emissions estimates were sensitive to both the retrieval data and the model setting used for the data assimilation. Different retrievals resulted in large discrepancies in the analyzed NO_x emissions. Thus, possible biases in the retrieval seriously degrade the emission analysis, with mean differences up to 60–70 % depending on the region. Furthermore, the observation minus forecast statistics showed significant diurnal variations. As a result of the uncertainty in the retrievals and in the diurnal variability scheme of the model, the use of different satellite products obtained at different overpass times causes large discrepancies in the emission estimates. In addition, the model performance in the upper troposphere (e.g., lightning NO₂ production) largely affected the emission estimation. Thus, it is important to consider both the model performance and retrieval dependence for better constraints on the NO_x sources.

In this study, only NO₂ data were assimilated to constrain the surface NO_x emissions. Multiple-species (e.g., HNO₃ and O₃) data obtained from various platforms can provide additional constraints through their chemical interactions. Meanwhile, only total emissions were adjusted from the data assimilation in this study. Sector-specific adjustments may help to explore the change in contributions of each emission source. It is also interesting to investigate the long-term variations of the emissions. Moreover, the surface NO_x emission estimate may be further improved by simultaneous optimization of atmospheric (e.g., lightning) and surface NO_x emissions, which impact the vertical distribution of NO_x sources. Advanced chemical data assimilation systems, such as developed by this study, make it possible to combine various data sets and to simultaneously optimize multiple model variables, including the atmospheric distribution of polluting trace gases and their precursor emissions.

Acknowledgements. We are grateful to Folkert Boersma, Vincent Huijnen, Hisashi Yashiro, and Masayuki Takigawa for their helpful discussions. This research was supported by the

Global NO_x emissions

K. Miyazaki et al.

Title Page

Abstract

Introduction

Conclusions

References

Tables

Figures

◀

▶

◀

▶

Back

Close

Full Screen / Esc

Printer-friendly Version

Interactive Discussion



References

- 5 Aksoy, A., Zhang, F., and Nielsen-Gammon, J. W.: Ensemble-based simultaneous state and parameter estimation in a two-dimensional sea-breeze model, *Mon. Weather Rev.*, 134, 2951–2970, doi:10.1175/MWR3224.1, 2006. 31536
- Anderson, J. L.: Spatially and temporally varying adaptive covariance inflation for ensemble filters, *Tellus A*, 61, 72–83, doi:10.1111/j.1600-0870.2008.00361.x, 2009. 31547
- 10 Blond, N., Boersma, K. F., Eskes, H. J., van der A, R. J., Van Roozendael, M., De Smedt, I., Bergametti, G., and Vautard, R.: Intercomparison of SCIAMACHY nitrogen dioxide observations, in situ measurements and air quality modeling results over Western Europe, *J. Geophys. Res.*, 112, 1–20, doi:10.1029/2006JD007277, 2007. 31530
- Boersma, K. F., Eskes, H. J., and Brinksma, E. J.: Error analysis for tropospheric NO₂ retrieval from space, *J. Geophys. Res.*, 109, D04311, doi:10.1029/2003JD003962, 2004. 31528, 31529
- 15 Boersma, K. F., Eskes, H. J., Meijer, E. W., and Kelder, H. M.: Estimates of lightning NO_x production from GOME satellite observations, *Atmos. Chem. Phys.*, 5, 2311–2331, doi:10.5194/acp-5-2311-2005, 2005. 31555
- Boersma, K. F., Eskes, H. J., Veefkind, J. P., Brinksma, E. J., van der A, R. J., Sneep, M., van den Oord, G. H. J., Levelt, P. F., Stammes, P., Gleason, J. F., and Bucsela, E. J.: Near-real time retrieval of tropospheric NO₂ from OMI, *Atmos. Chem. Phys.*, 7, 2103–2118, doi:10.5194/acp-7-2103-2007, 2007. 31528, 31529, 31530
- 20 Boersma, K. F., Jacob, D. J., Eskes, H. J., Pinder, R. W., Wang, J., and van der A, R. J.: Intercomparison of SCIAMACHY and OMI tropospheric NO₂ columns: Observing the diurnal evolution of chemistry and emissions from space, *J. Geophys. Res.*, 113, 1–14, doi:10.1029/2007JD008816, 2008. 31526, 31533, 31542, 31544, 31553
- Boersma, K. F., Eskes, H. J., Dirksen, R. J., van der A, R. J., Veefkind, J. P., Stammes, P., Huijnen, V., Kleipool, Q. L., Sneep, M., Claas, J., Leitão, J., Richter, A., Zhou, Y., and Brunner, D.: An improved tropospheric NO₂ column retrieval algorithm for the Ozone Monitoring Instrument, *Atmos. Meas. Tech.*, 4, 1905–1928, doi:10.5194/amt-4-1905-2011, 2011. 31529
- 30

Global NO_x emissions

K. Miyazaki et al.

Title Page

Abstract

Introduction

Conclusions

References

Tables

Figures

◀

▶

◀

▶

Back

Close

Full Screen / Esc

Printer-friendly Version

Interactive Discussion



**Global NO_x
emissions**

K. Miyazaki et al.

Title Page

Abstract

Introduction

Conclusions

References

Tables

Figures

◀

▶

◀

▶

Back

Close

Full Screen / Esc

Printer-friendly Version

Interactive Discussion



- Bovensmann, H., Burrows, J. P., Buchwitz, M., Frerick, J., Noel, S., Rozanov, V. V., Chance, K. V., and Goede, A. P. H.: SCIAMACHY: mission objectives and measurement modes, *J. Atmos. Sci.*, 56, 127–150, 1999. 31529
- 5 Bucselá, E. J., Perring, a. E., Cohen, R. C., Boersma, K. F., Celarier, E. a., Gleason, J. F., Wenig, M. O., Bertram, T. H., Wooldridge, P. J., Dirksen, R., and Veefkind, J. P.: Comparison of tropospheric NO₂ from in situ aircraft measurements with near-real-time and standard product data from OMI, *J. Geophys. Res.*, 113, 1–14, doi:10.1029/2007JD008838, 2008. 31530
- 10 Chai, T., Carmichael, G. R., Tang, Y., Sandu, A., Heckel, A., Richter, A., and Burrows, J. P.: Regional NO_x emission inversion through a four-dimensional variational approach using SCIAMACHY tropospheric NO₂ column observations, *Atmos. Env.*, 43, 5046–5055, doi:10.1016/j.atmosenv.2009.06.052, 2009. 31526, 31537
- Eskes, H. J. and Boersma, K. F.: Averaging kernels for DOAS total-column satellite retrievals, *Atmos. Chem. Phys.*, 3, 1285–1291, doi:10.5194/acp-3-1285-2003, 2003. 31528, 31536
- 15 Eskes, H. J., Velthoven, P. F. J. V., Valks, P. J. M., and Kelder, H. M.: Assimilation of GOME total-ozone satellite observations in a three-dimensional tracer-transport model, *Q. J. Roy. Meteorol. Soc.*, 129, 1663–1681, doi:10.1256/qj.02.14, 2003. 31539
- Evensen, G.: Sequential data assimilation with a nonlinear quasi-geostrophic model using Monte Carlo methods to forecast error statistics, *J. Geophys. Res.*, 99, 10143–10162, doi:10.1029/94JC00572, 1994. 31526
- 20 Graedel, T. E., Bates, T. S., Bouwman, A. F., Cunnold, D., Dignon, J., Fung, I., Jacob, D. J., Lamb, B. K., Logan, J. A., Marland, G., Middleton, P., Pacyna, J. M., Placet, M., and Veldt, C.: A compilation of inventories of emissions to the atmosphere, *Global Biogeochem. Cy.*, 7, 1–26, 1993. 31532
- 25 Houtekamer, P. L. and Mitchell, H. L.: Data assimilation using an ensemble Kalman filter technique, *Mon. Weather Rev.*, 126, 796–811, doi:10.1175/1520-0493(1998)126(0796:DAUAEK)2.0.CO;2, 1998. 31535
- Houtekamer, P. L. and Mitchell, H. L.: A sequential ensemble Kalman filter for atmospheric data assimilation, *Mon. Weather Rev.*, 129, 123–137, doi:10.1175/1520-0493(2001)129(0123:ASEKFF)2.0.CO;2, 2001. 31535
- 30 Huijnen, V., Williams, J., van Weele, M., van Noije, T., Krol, M., Dentener, F., Segers, A., Houweling, S., Peters, W., de Laat, J., Boersma, F., Bergamaschi, P., van Velthoven, P., Le Sager, P., Eskes, H., Alkemade, F., Scheele, R., Nédélec, P., and Pätz, H.-W.: The global

**Global NO_x
emissions**

K. Miyazaki et al.

Title Page

Abstract

Introduction

Conclusions

References

Tables

Figures

◀

▶

◀

▶

Back

Close

Full Screen / Esc

Printer-friendly Version

Interactive Discussion



chemistry transport model TM5: description and evaluation of the tropospheric chemistry version 3.0, *Geosci. Model Dev.*, 3, 445–473, doi:10.5194/gmd-3-445-2010, 2010. 31542

Hunt, B. R., Kostelich, E. J., and Szunyogh, I.: Efficient data assimilation for spatiotemporal chaos: a local ensemble transform Kalman filter, *Physica D*, 230, 112–126, 2007. 31526, 31534, 31535

IPCC: Climate Change 2007, The Physical Science Basis, Cambridge University Press, Cambridge, United Kingdom and New York, NY, USA, 2007. 31524

Jaeglé, L., Steinberger, L., Martin, R. V., and Chance, K.: Global partitioning of NO_x sources using satellite observations: Relative roles of fossil fuel combustion, biomass burning and soil emissions, *Faraday Discuss.*, 130, 407–423, 2005. 31550

Kalnay, E.: Ensemble Kalman filter: current status and potential, in: *Data Assimilation: Making Sense of Observations*, edited by: Lahoz, W., Khatatov, B., and Ménard, R., Springer, Berlin, Heidelberg, Germany, 69–92, 2010. 31534

Kanamitsu, M., Ebisuzaki, W., Woollen, J., Yang, S.-K., Hnilo, J. J., Fiorino, M., and Potter, G. L.: NCEP-DOE AMIP-II Reanalysis (R-2), *B. Am. Meteorol. Soc.*, 83, 1631–1643, doi:10.1175/BAMS-83-11-1631, 2002. 31532

Kurokawa, J.-i., Yumimoto, K., Uno, I., and Ohara, T.: Adjoint inverse modeling of NO_x emissions over Eastern China using satellite observations of NO₂ vertical column densities, *Atmos. Env.*, 43, 1878–1887, doi:10.1016/j.atmosenv.2008.12.030, 2009. 31526, 31537, 31547

Lamsal, L. N., Martin, R. V., van Donkelaar, A., Celarier, E. a., Bucsela, E. J., Boersma, K. F., Dirksen, R., Luo, C., and Wang, Y.: Indirect validation of tropospheric nitrogen dioxide retrieved from the OMI satellite instrument: insight into the seasonal variation of nitrogen oxides at northern midlatitudes, *J. Geophys. Res.*, 115, 1–15, doi:10.1029/2009JD013351, 2010. 31525, 31526, 31527, 31529, 31543, 31550

Levelt, P. F., Hilsenrath, E., Leppelmeier, G. W., Van Den Oord, G. H. J., Bhartia, P. K., Tamminen, J., De Haan, J. F., and Veeckind, P.: Science objectives of the ozone monitoring instrument, *Geosci. Remote Sens.*, 44, 1199–1208, doi:10.1109/TGRS.2006.872336, 2006. 31528

Lin, J.-T., McElroy, M. B., and Boersma, K. F.: Constraint of anthropogenic NO_x emissions in China from different sectors: a new methodology using multiple satellite retrievals, *Atmos. Chem. Phys.*, 10, 63–78, doi:10.5194/acp-10-63-2010, 2010. 31526, 31530, 31555

Martin, R., Jacob, D., Chance, K., Kurosu, T., Palmer, P., and Evans, M.: Global inventory

**Global NO_x
emissions**

K. Miyazaki et al.

Title Page

Abstract

Introduction

Conclusions

References

Tables

Figures

◀

▶

◀

▶

Back

Close

Full Screen / Esc

Printer-friendly Version

Interactive Discussion



- of nitrogen oxide emissions constrained by space-based observations of NO₂ columns, *J. Geophys. Res.*, 108, 1–12, doi:10.1029/2003JD003453, 2003. 31526, 31536, 31537, 31550
- Ménard, R. and Chang, L.-P.: Assimilation of stratospheric chemical tracer observations using a Kalman filter. Part II: χ^2 -validated results and analysis of variance and correlation dynamics, *Mon. Weather Rev.*, 128, 2672–2686, 2000. 31546
- Miyoshi, T. and Yamane, S.: Local ensemble transform Kalman filtering with an AGCM at a T159/L48 resolution, *Mon. Weather Rev.*, 135, 3841–3861, doi:10.1175/2007MWR1873.1, 2007. 31534, 31536
- Müller, J.-F. and Stavrou, T.: Inversion of CO and NO_x emissions using the adjoint of the IMAGES model, *Atmos. Chem. Phys.*, 5, 1157–1186, doi:10.5194/acp-5-1157-2005, 2005. 31526, 31550
- Nagashima, T., Ohara, T., Sudo, K., and Akimoto, H.: The relative importance of various source regions on East Asian surface ozone, *Atmos. Chem. Phys.*, 10, 11305–11322, doi:10.5194/acp-10-11305-2010, 2010. 31532
- Napelenok, S. L., Pinder, R. W., Gilliland, A. B., and Martin, R. V.: A method for evaluating spatially-resolved NO_x emissions using Kalman filter inversion, direct sensitivities, and space-based NO₂ observations, *Atmos. Chem. Phys.*, 8, 5603–5614, doi:10.5194/acp-8-5603-2008, 2008. 31555
- Ohara, T., Akimoto, H., Kurokawa, J., Horii, N., Yamaji, K., Yan, X., and Hayasaka, T.: An Asian emission inventory of anthropogenic emission sources for the period 1980–2020, *Atmos. Chem. Phys.*, 7, 4419–4444, doi:10.5194/acp-7-4419-2007, 2007. 31532
- Olivier, J. G. J., Van Aardenne, J. A., Dentener, F., Pagliari, V., Ganzeveld, L. N., and Peters, J. A. H. W.: Recent trends in global greenhouse gas emissions: regional trends 1970–2000 and spatial distribution of key sources in 2000, *Environ. Sci.*, 2, 81–99, 2005. 31532
- Ott, E., Hunt, B. R., Szunyogh, I., Zimin, A. V., Kostelich, E. J., Corazza, M., Kalnay, E., Patil, D. J., and Yorke, J. A.: A local ensemble Kalman filter for atmospheric data assimilation, *Tellus A*, 56, 415–428, doi:10.1111/j.1600-0870.2004.00076.x, 2004. 31534
- Price, C. and Rind, D.: A simple lightning parameterization for calculating global lightning distributions, *J. Geophys. Res.*, 97, 9919–9933, 1992. 31532
- Randerson, J. T., van der Werf, G. R., Giglio, L., Collatz, G. J., and Kasibhatla, P. S.: Global Fire Emissions Database, Version 2 (GFEDv2.1). Data set, available at: <http://daac.ornl.gov/>, July 2011, 2007. 31532
- Richter, A.: Satellite measurements of NO₂ from international shipping emissions, *Geophys.*

**Global NO_x
emissions**

K. Miyazaki et al.

[Title Page](#)[Abstract](#)[Introduction](#)[Conclusions](#)[References](#)[Tables](#)[Figures](#)[◀](#)[▶](#)[◀](#)[▶](#)[Back](#)[Close](#)[Full Screen / Esc](#)[Printer-friendly Version](#)[Interactive Discussion](#)

Res. Lett., 31, 4–7, doi:10.1029/2004GL020822, 2004. 31526

Schaub, D., Brunner, D., Boersma, K. F., Keller, J., Folini, D., Buchmann, B., Berresheim, H., and Staehelin, J.: SCIAMACHY tropospheric NO₂ over Switzerland: estimates of NO_x lifetimes and impact of the complex Alpine topography on the retrieval, Atmos. Chem. Phys., 7, 5971–5987, doi:10.5194/acp-7-5971-2007, 2007. 31530

Singh, H. B., Brune, W. H., Crawford, J. H., Flocke, F., and Jacob, D. J.: Chemistry and transport of pollution over the Gulf of Mexico and the Pacific: spring 2006 INTEX-B campaign overview and first results, Atmos. Chem. Phys., 9, 2301–2318, doi:10.5194/acp-9-2301-2009, 2009. 31530

Stavrakou, T., Müller, J.-F., Boersma, K. F., De Smedt, I., and van der A, R. J.: Assessing the distribution and growth rates of NO_x emission sources by inverting a 10-year record of NO₂ satellite columns, Geophys. Res. Lett., 35, 1–5, doi:10.1029/2008GL033521, 2008. 31526

Streets, D. G., Bond, T. C., Carmichael, G. R., Fernandes, S. D., Fu, Q., He, D., Klimont, Z., Nelson, S. M., Tsai, N. Y., Wang, M. Q., Woo, J. H., and Yarber, K. F.: An inventory of gaseous and primary aerosol emissions in Asia in the year 2000, J. Geophys. Res., 108, 8809, doi:10.1029/2002JD003093, 2003. 31525

Sudo, K. and Akimoto, H.: Global source attribution of tropospheric ozone: Long-range transport from various source regions, J. Geophys. Res., 112, D12302, doi:10.1029/2006JD007992, 2007. 31532

Sudo, K., Takahashi, M., and Akimoto, H.: CHASER: A global chemical model of the troposphere 2. Model results and evaluation, J. Geophys. Res., 107, doi:10.1029/2001JD001114, 2002a. 31532

Sudo, K., Takahashi, M., Kurokawa, J., and Akimoto, H.: CHASER: A global chemical model of the troposphere 1. Model description, J. Geophys. Res., 107, 4339, doi:10.1029/2001JD001113, 2002b. 31527, 31531, 31532

Thornton, J. A., Wooldridge, P. J., Cohen, R. C., Williams, E. J., Hereid, D., Fehsenfeld, F. C., Stutz, J., and Alicke, B.: Comparisons of in situ and long path measurements of NO₂ in urban plumes, J. Geophys. Res., 108, 4496, doi:10.1029/2003JD003559, 2003. 31530

Van der A, R. J., Peters, D. H. M. U., Eskes, H., Boersma, K. F., Van Roozendaal, M., De Smedt, I., and Kelder, H. M.: Detection of the trend and seasonal variation in tropospheric NO₂ over China, J. Geophys. Res., 111, 1–10, doi:10.1029/2005JD006594, 2006. 31526

Van der A, R. J., Eskes, H. J., Boersma, K. F., van Noije, T. P. C., Van Roozendaal, M., De Smedt, I., Peters, D. H. M. U., and Meijer, E. W.: Trends, seasonal variability and dominant

**Global NO_x
emissions**

K. Miyazaki et al.

[Title Page](#)[Abstract](#)[Introduction](#)[Conclusions](#)[References](#)[Tables](#)[Figures](#)[◀](#)[▶](#)[◀](#)[▶](#)[Back](#)[Close](#)[Full Screen / Esc](#)[Printer-friendly Version](#)[Interactive Discussion](#)

NO_x source derived from a ten year record of NO₂ measured from space, *J. Geophys. Res.*, 113, 1–12, doi:10.1029/2007JD009021, 2008. 31526, 31533

van Noije, T. P. C., Eskes, H. J., Dentener, F. J., Stevenson, D. S., Ellingsen, K., Schultz, M. G., Wild, O., Amann, M., Atherton, C. S., Bergmann, D. J., Bey, I., Boersma, K. F., Butler, T., Cofala, J., Drevet, J., Fiore, A. M., Gauss, M., Hauglustaine, D. A., Horowitz, L. W., Isak-
5 sen, I. S. A., Krol, M. C., Lamarque, J.-F., Lawrence, M. G., Martin, R. V., Montanaro, V., Müller, J.-F., Pitari, G., Prather, M. J., Pyle, J. A., Richter, A., Rodriguez, J. M., Savage, N. H., Strahan, S. E., Sudo, K., Szopa, S., and van Roozendaal, M.: Multi-model ensemble simula-
10 tions of tropospheric NO₂ compared with GOME retrievals for the year 2000, *Atmos. Chem. Phys.*, 6, 2943–2979, doi:10.5194/acp-6-2943-2006, 2006. 31527, 31532, 31541, 31542, 31544, 31547

Velders, G., Granier, C., Portmann, R., Pfeilsticker, K., Wenig, M., Wagner, T., Platt, U., Richter, A., and Burrows, J.: Global tropospheric NO₂ column distributions – comparing
15 three-dimensional model calculations with GOME measurements, *J. Geophys. Res.*, 106, 12, 2001. 31525, 31543

Volten, H., Brinksma, E. J., Berkhout, A. J. C., Hains, J., Bergwerff, J. B., Van der Hoff, G. R., Apituley, A., Dirksen, R. J., Calabretta-Jongen, S., and Swart, D. P. J.: NO₂ lidar pro-
20 file measurements for satellite interpretation and validation, *J. Geophys. Res.*, 114, 1–18, doi:10.1029/2009JD012441, 2009. 31531

Wang, Y., McElroy, M. B., Martin, R. V., Streets, D. G., Zhang, Q., and Fu, T.-M.: Sea-
25 sonal variability of NO_x emissions over East China constrained by satellite observa- tions: implications for combustion and microbial sources, *J. Geophys. Res.*, 112, 1–19, doi:10.1029/2006JD007538, 2007. 31525, 31537

Yienger, J. and Levy, H.: Empirical model of global soil-biogenic NO_x emissions, *J. Geophys. Res.*, 100, 11447–11464, 1999. 31533

Zhao, C. and Wang, Y.: Assimilated inversion of NO_x emissions over East Asia using OMI NO₂
30 column measurements, *Geophys. Res. Lett.*, 36, 1–5, doi:10.1029/2008GL037123, 2009. 31526, 31537

Zupanski, D. and Zupanski, M.: Model error estimation employing an ensemble data assimila-
tion approach, *Mon. Weather Rev.*, 134, 1337–1354, doi:10.1175/MWR3125.1, 2006. 31546

Global NO_x
emissions

K. Miyazaki et al.

Table 1. Comparisons of monthly and annual mean tropospheric NO₂ columns between the CHASER simulation (with applying the AK of each retrieval) and the satellite retrievals: DOMINO v1, DOMINO v2, and SCIAMACHY, for 2005. The RMSE is the root-mean-square error. The bias represents the CHASER simulation minus the retrievals. The units for the RMSE and bias are 10¹⁵ mol cm⁻².

		Jan	Apr	Jul	Oct	Ann
vs. DOMINO v2	Corr	0.71	0.88	0.90	0.88	0.86
	RMSE	0.79	0.36	0.28	0.41	0.38
	Bias	-0.01	-0.02	-0.07	-0.08	-0.03
vs. DOMINO v1	Corr	0.77	0.88	0.89	0.89	0.89
	RMSE	0.92	0.44	0.31	0.48	0.44
	Bias	-0.11	-0.07	-0.07	-0.12	-0.06
vs. SCIAMACHY	Corr	0.76	0.82	0.79	0.80	0.86
	RMSE	1.03	0.57	0.51	0.53	0.53
	Bias	-0.06	0.06	0.04	0.00	0.01

Title Page

Abstract

Introduction

Conclusions

References

Tables

Figures

I◀

▶I

◀

▶

Back

Close

Full Screen / Esc

Printer-friendly Version

Interactive Discussion



Global NO_x
emissions

K. Miyazaki et al.

Table 2. The performance of the data assimilation for different parameters: the horizontal localization length (loc in km), the covariance inflation (inf in %), and the ensemble number (num). Five-day mean (averaged over 7–11 January 2005) tropospheric NO₂ columns from the assimilation and from DOMINO v2 are compared. Corr is the global spatial correlation coefficient and RMSE is the root-mean-square error in 10¹⁵ mol cm⁻². The control (CTL) simulation was conducted with loc = 450, inf = 5, and num = 32.

	Corr	RMSE
CTL	0.906	0.599
loc = 300	0.906	0.600
loc = 600	0.897	0.625
loc = 750	0.885	0.645
loc = 900	0.879	0.655
num = 16	0.897	0.612
num = 48	0.906	0.597
num = 64	0.905	0.597
inf = 0	0.904	0.605
inf = 10	0.904	0.607
inf = 15	0.905	0.589

[Title Page](#)[Abstract](#)[Introduction](#)[Conclusions](#)[References](#)[Tables](#)[Figures](#)[I◀](#)[▶I](#)[◀](#)[▶](#)[Back](#)[Close](#)[Full Screen / Esc](#)[Printer-friendly Version](#)[Interactive Discussion](#)

Global NO_x
emissions

K. Miyazaki et al.

Title Page

Abstract

Introduction

Conclusions

References

Tables

Figures

I◀

▶I

◀

▶

Back

Close

Full Screen / Esc

Printer-friendly Version

Interactive Discussion



Table 3. The four-month mean (January, April, July, and October in 2005) global and regional NO_x emissions (in Tg N yr⁻¹) obtained from the a priori emissions, the a posteriori emissions with DOMINO v2 data, and the latest inventories (EDGAR4.1 + GFED3.1 + GEIA).

	A priori	A posteriori
E-China	3.1	5.0
Europe	5.5	4.6
E-USA	2.6	3.4
S-America	0.7	1.1
N-Africa	3.1	2.6
C-Africa	2.0	1.9
S-Africa	0.2	0.5
SE-Asia	0.4	0.7
Northern Hemisphere (20–90° N)	27.1	29.3
Tropics (20° S–20° N)	11.9	12.0
Southern Hemisphere (20–90° S)	2.7	4.1
Globe	41.6	45.4

Global NO_x
emissions

K. Miyazaki et al.

Table 4. Comparisons of tropospheric NO₂ columns between the data assimilation run and the satellite retrievals DOMINO v2 (OMI) and SCIAMACHY (SCIA). The results are obtained from 15-day averages (from the 16th to the 30th of each month) provided for four months in 2005. Shown are the global spatial correlation (Corr), the root-mean-square error (RMSE), and the mean bias in 10¹⁵ mol cm⁻². The model simulation results (without data assimilation) are also shown in brackets.

		Jan	Apr	Jul	Oct
vs. OMI	S-Corr	0.92 (0.73)	0.93 (0.87)	0.93 (0.89)	0.95 (0.86)
	RMSE	0.50 (0.82)	0.28 (0.38)	0.23 (0.30)	0.29 (0.45)
	Bias	0.01 (−0.01)	0.02 (−0.02)	0.00 (−0.04)	−0.03 (−0.07)
vs. SCIA	S-Corr	0.87 (0.77)	0.84 (0.81)	0.81 (0.76)	0.86 (0.77)
	RMSE	0.85 (1.11)	0.54 (0.60)	0.52 (0.58)	0.49 (0.61)
	Bias	−0.01 (−0.06)	0.14 (0.09)	0.08 (0.04)	0.10 (0.06)

Title Page

Abstract

Introduction

Conclusions

References

Tables

Figures

I◀

▶I

◀

▶

Back

Close

Full Screen / Esc

Printer-friendly Version

Interactive Discussion



Global NO_x
emissions

K. Miyazaki et al.

Table 5. The 15-days mean (averaged over the 16–30 of each month) bias of regional mean tropospheric NO₂ columns; the data assimilation run minus the satellite retrievals (DOMINO v2 (OMI) and SCIAMACHY (SCIA)) in 10¹⁵ mol cm⁻², for four months in 2005. The model simulation results (without data assimilation) are also shown in brackets.

		Jan	Apr	Jul	Oct
E-China	vs. OMI	-0.67 (-4.58)	-0.19 (-1.64)	-0.08 (-0.78)	-0.53 (-2.42)
	vs. SCIA	-1.37 (-7.24)	-0.64 (-2.54)	-0.77 (-1.93)	-1.09 (-2.85)
Europe	vs. OMI	-0.12 (0.84)	-0.40 (-0.35)	-0.09 (-0.26)	-0.31 (-0.25)
	vs. SCIA	-0.58 (0.08)	-0.21 (-0.11)	0.07 (-0.04)	0.29 (0.36)
E-USA	vs. OMI	-1.92 (-2.65)	-0.96 (-1.68)	-0.04 (-0.31)	-0.52 (-1.46)
	vs. SCIA	-4.79 (-5.40)	-0.92 (-1.85)	-0.23 (-0.52)	-0.78 (-1.63)
S-America	vs. OMI	0.02 (-0.03)	0.05 (0.02)	-0.06 (0.10)	0.03 (-0.43)
	vs. SCIA	0.09 (0.05)	0.54 (0.49)	0.03 (0.15)	-0.02 (-0.43)
N-Africa	vs. OMI	0.12 (0.15)	0.11 (-0.07)	-0.11 (-0.22)	-0.04 (0.05)
	vs. SCIA	-0.07 (-0.07)	0.21 (0.19)	-0.12 (-0.21)	0.18 (0.29)
C-Africa	vs. OMI	-0.17 (-0.25)	0.13 (-0.05)	-0.19 (-0.27)	-0.37 (-0.50)
	vs. SCIA	-0.22 (-0.31)	0.30 (0.02)	-0.48 (-0.54)	-0.33 (-0.43)
S-Africa	vs. OMI	-0.54 (-0.73)	-1.17 (-1.42)	-1.58 (-2.80)	-0.74 (-1.38)
	vs. SCIA	-2.16 (-2.47)	-2.74 (-3.02)	-3.42 (-4.73)	-0.54 (-1.79)
SE-Asia	vs. OMI	-0.01 (-0.32)	-0.14 (-0.44)	0.16 (-0.09)	-0.09 (-0.15)
	vs. SCIA	0.24 (-0.21)	-0.29 (-0.54)	0.18 (0.16)	0.19 (0.17)

Title Page

Abstract

Introduction

Conclusions

References

Tables

Figures

◀

▶

◀

▶

Back

Close

Full Screen / Esc

Printer-friendly Version

Interactive Discussion



Global NO_x
emissions

K. Miyazaki et al.

Table 6. The 15-day mean (16–30 of each month) and regional mean relative observation error for DOMINO v2. The relative error was estimated by dividing the mean observation error by the mean observation concentration for each super-observation. The mean number of OMI pixels (per day per 1.0° × 1.0°) used for making the super-observation is shown in brackets. Note that during the calculation of the relative error, 0.1 × 10¹⁵ mol cm⁻² was added to both the denominator and the numerator to avoid the divergence caused by near-zero concentrations and to reduce the influence of remote site data.

	Jan	Apr	Jul	Oct
E-China	1.1 (8.6)	0.9 (17.0)	0.5 (9.2)	1.0 (14.3)
Europe	1.1 (9.8)	1.5 (13.7)	1.0 (15.6)	1.5 (15.0)
E-USA	0.7 (10.5)	0.9 (13.4)	0.5 (17.3)	0.9 (16.5)
S-America	1.5 (5.4)	2.0 (6.2)	1.6 (20.5)	1.2 (7.9)
N-Africa	1.2 (22.7)	1.4 (17.2)	0.9 (15.9)	1.2 (20.2)
C-Africa	1.3 (10.8)	1.5 (14.9)	0.9 (19.7)	0.8 (10.1)
S-Africa	1.0 (6.3)	1.0 (13.6)	0.9 (25.5)	0.8 (15.9)
SE-Asia	1.0 (24.4)	0.9 (16.1)	1.9 (2.9)	1.3 (11.1)

Title Page

Abstract

Introduction

Conclusions

References

Tables

Figures

I◀

▶I

◀

▶

Back

Close

Full Screen / Esc

Printer-friendly Version

Interactive Discussion



Global NO_x
emissions

K. Miyazaki et al.

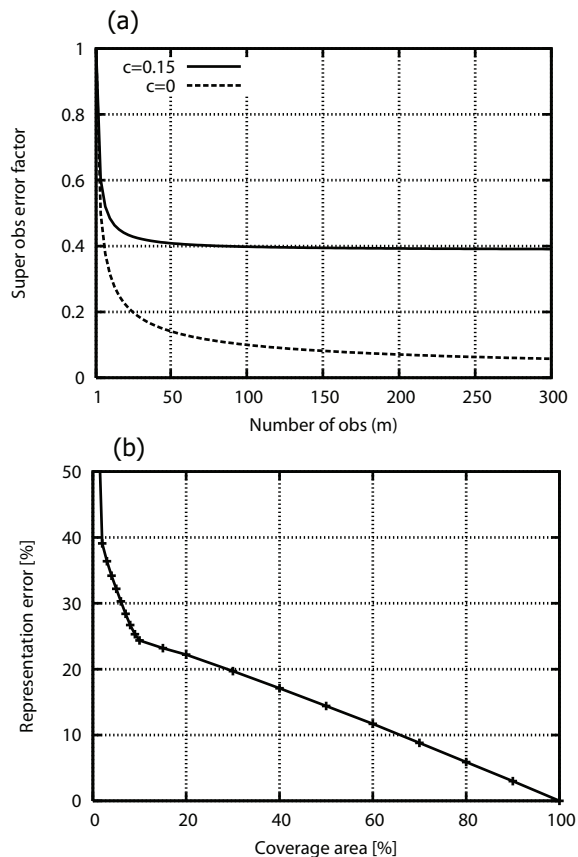


Fig. 1. (a, top panel) The error reduction factor for the super-observation as a function of number of observations, m , for different sub-grid error correlations, $c = 0$ (dotted line) and 15% (solid line). (b, bottom panel) The representativeness error multiplication factor f_{rep} as a function of the coverage of the grid cell by OMI observations. See Eq. (10) and Sect. 2.3.3 for details.

Global NO_x
emissions

K. Miyazaki et al.

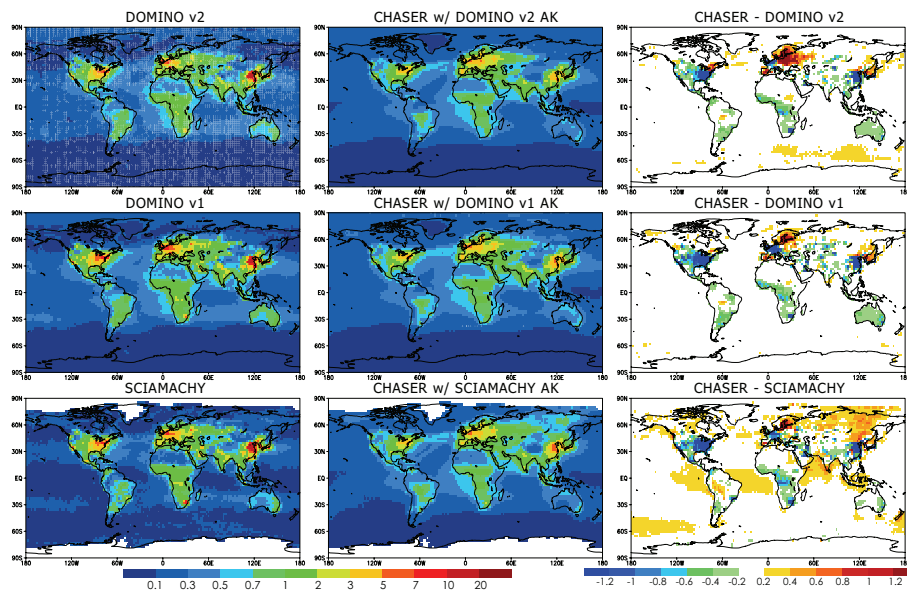


Fig. 2. Global distributions of annual mean tropospheric NO₂ columns (in 10^{15} mol cm⁻²) obtained from the satellite retrievals (left columns): DOMINO v2 (upper rows), DOMINO v1 (middle rows), and SCIAMACHY (lower rows), and the CHASER simulation calculated with the AK for each retrieval (middle columns) for 2005. The differences between the retrievals and the CHASER simulation (the simulation minus the retrievals) are shown in the right columns; the red (blue) colour indicates that the CHASER is larger (smaller) than the satellite retrievals.

Title Page

Abstract

Introduction

Conclusions

References

Tables

Figures

◀

▶

◀

▶

Back

Close

Full Screen / Esc

Printer-friendly Version

Interactive Discussion



Global NO_x
emissions

K. Miyazaki et al.

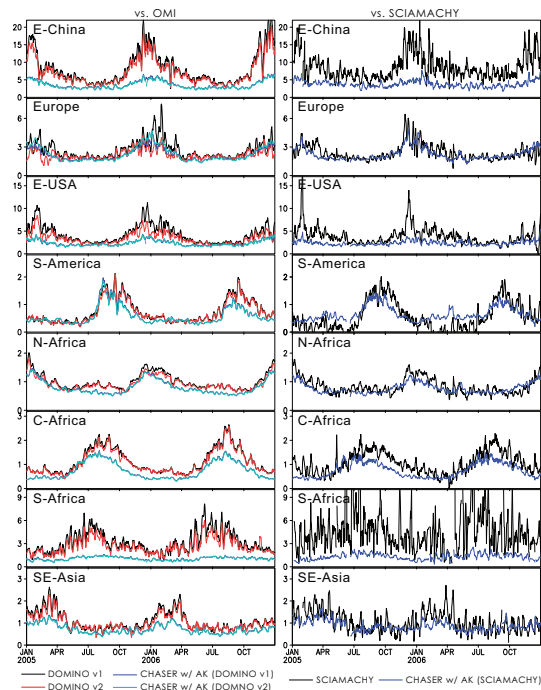


Fig. 3. Seasonal variations of the regional mean tropospheric NO₂ columns (in 10^{15} mol cm⁻²) for Eastern China (110–123° E, 30–40° N, top panels), Europe (10° W–30° E, 35–60° N, second-top panels), the Eastern United States (95–71° W, 32–43° N, third-top panels), South America (70–50° W, 20° S–Equator, fourth-top panels), Northern Africa (20° W–40° E, Equator–20° N, fifth-top panels), Central Africa (10–40° E, 20° S–Equator, sixth-top panels), Southern Africa (26–31° E, 28–23° S, seventh-top panels), and Southeast Asia (96–105° E, 10–20° N, bottom panels) for 2005–2006. Tropospheric NO₂ columns obtained from DOMINO v2 (red lines in left panels), DOMINO v1 (black lines in left panels), the SCIAMACHY retrieval (black lines in right panels), and the CHASER simulation with the AK (blue and light blue lines) are plotted for local time 13:30 (left) and 10:00 (right). A 4-day running-mean was applied to the data.

Title Page

Abstract

Introduction

Conclusions

References

Tables

Figures

◀

▶

◀

▶

Back

Close

Full Screen / Esc

Printer-friendly Version

Interactive Discussion



Global NO_x
emissions

K. Miyazaki et al.

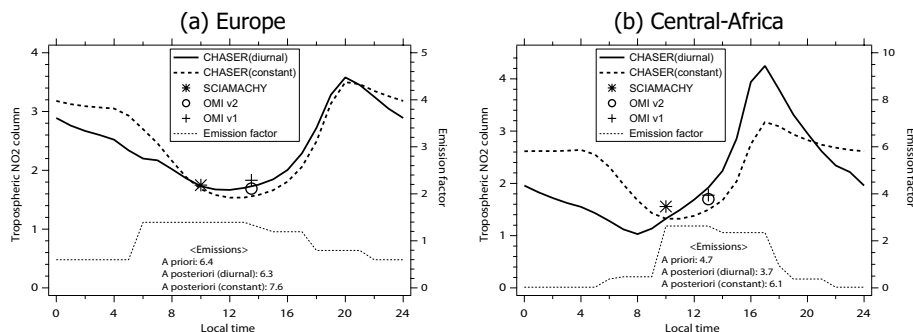


Fig. 4. Monthly mean diurnal variation of tropospheric NO₂ columns (in 10¹⁵ mol cm⁻²) obtained from the CHASER simulation with (solid line) and without (broken line) the diurnal variability scheme for surface NO_x emissions over (a) Europe (10° W–30° E, 35–60° N) and (b) Central Africa (10–40° E, 20° S–Equator) in July 2005. Tropospheric NO₂ columns obtained from the satellite retrievals: DOMINO v1 (cross), DOMINO v2 (circle), and SCIAMACHY (asterisk) are also plotted. The dotted line represents the diurnal variability factor used for NO_x emissions.

Title Page

Abstract

Introduction

Conclusions

References

Tables

Figures

◀

▶

◀

▶

Back

Close

Full Screen / Esc

Printer-friendly Version

Interactive Discussion



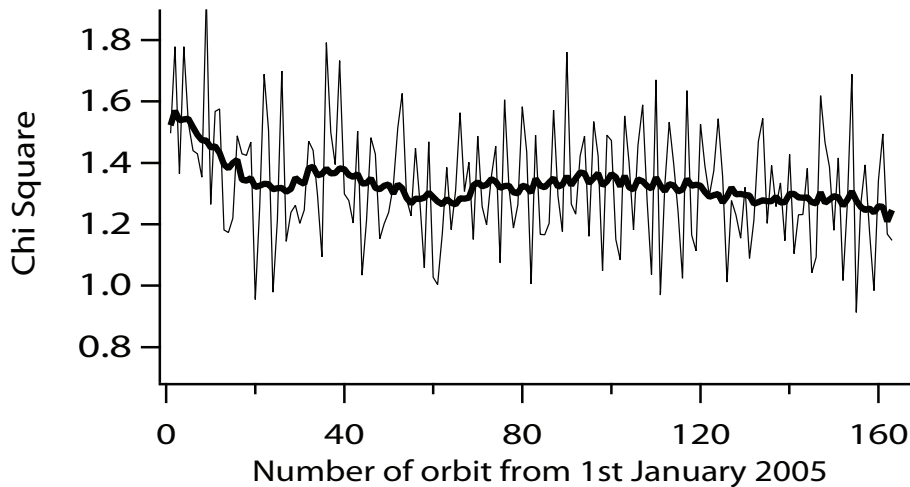


Fig. 5. Temporal variation of the χ square calculated as values estimated in each data assimilation cycle (thin line) and 15-orbit cycle running means (bold line).

Global NO_x emissions

K. Miyazaki et al.

Title Page	
Abstract	Introduction
Conclusions	References
Tables	Figures
◀	▶
◀	▶
Back	Close
Full Screen / Esc	
Printer-friendly Version	
Interactive Discussion	



Global NO_x
emissions

K. Miyazaki et al.

Title Page

Abstract

Introduction

Conclusions

References

Tables

Figures

◀

▶

◀

▶

Back

Close

Full Screen / Esc

Printer-friendly Version

Interactive Discussion

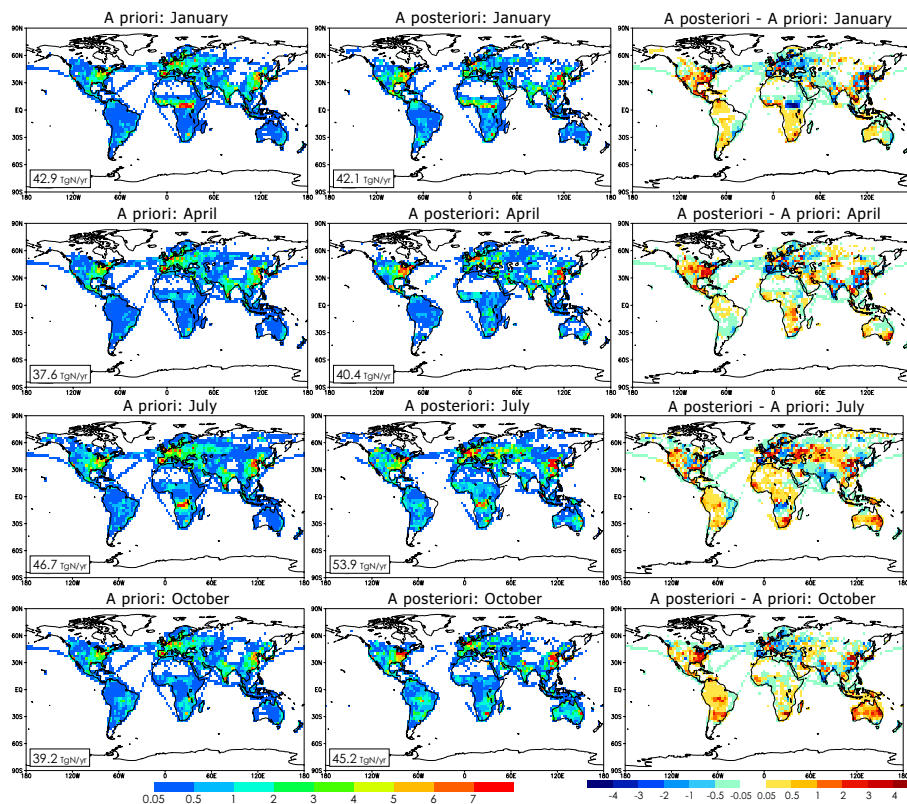


Fig. 6. Global distributions of the surface NO_x emissions (in kg m⁻² s⁻¹), averaged over the 16–30 of each month, obtained from the a priori emissions (left columns), the a posteriori emissions (the data assimilation results, center columns), and the difference between them (the a posteriori emissions minus the a priori emissions, right columns) in January, April, July, and October 2005. The red (blue) colour in the right panels indicates that the data assimilation increases (decreases) the surface NO_x emissions.

Global NO_x emissions

K. Miyazaki et al.

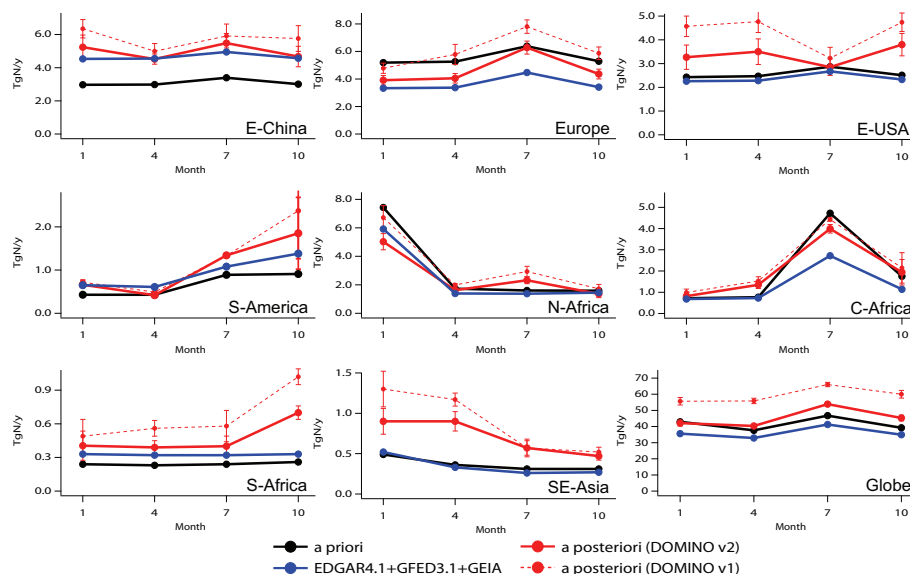


Fig. 7. Seasonal variations of the regional and global surface NO_x emissions (in Tg Nyr⁻¹) obtained from the a priori emissions (black lines), the a posteriori emissions with DOMINO v2 data (red solid line) and DOMINO v1 data (red dotted line), and the latest inventories (EDGAR4.1+GFED3.1+GEIA, blue lines), averaged over the 16–30 of each month in January, April, July, and October 2005. The error bars represent the standard deviations of the a posteriori emissions during the analysis period. The results are shown for Eastern China (top left panel), Europe (top center panel), the Eastern United States (top right panel), South America (middle left panel), Northern Africa (middle center panel), Central Africa (middle right panel), Southern Africa (bottom left panel), and Southeast Asia (bottom center panel), and the globe (bottom right panel).

Title Page

Abstract	Introduction
Conclusions	References
Tables	Figures

◀
▶

◀
▶

Back
Close

Full Screen / Esc

Printer-friendly Version

Interactive Discussion



Global NO_x
emissions

K. Miyazaki et al.

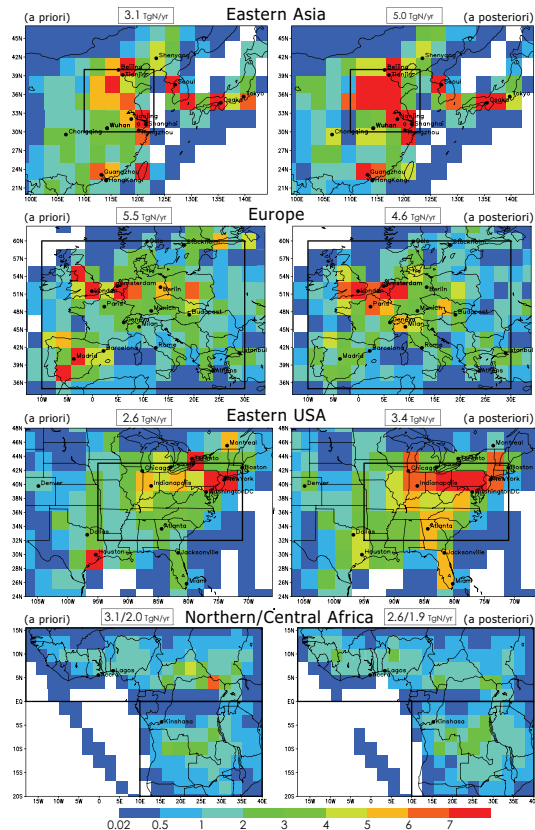


Fig. 8. Same as Fig. 6, but showing the regional distribution over Eastern Asia (upper panels), Europe (upper middle panels), the Eastern United States (lower middle panels), and Central Africa (lower panels), obtained from the a priori emissions (left panels) and the a posteriori emissions (right panels), averaged over four months, January, April, July, and October, in 2005. The black square line represents the region used for the regional mean analysis; the number shown in the top of the panels represents the total NO_x emission for the regional domain.

Title Page

Abstract

Introduction

Conclusions

References

Tables

Figures

◀

▶

◀

▶

Back

Close

Full Screen / Esc

Printer-friendly Version

Interactive Discussion



Global NO_x
emissions

K. Miyazaki et al.

Title Page

Abstract

Introduction

Conclusions

References

Tables

Figures

◀

▶

◀

▶

Back

Close

Full Screen / Esc

Printer-friendly Version

Interactive Discussion

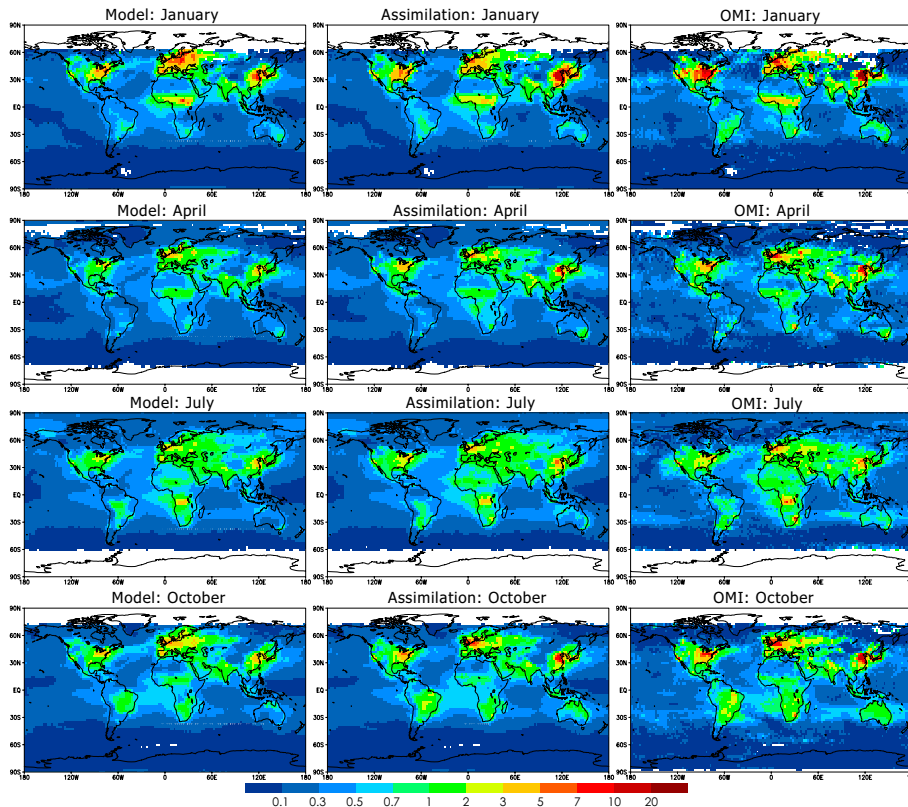


Fig. 9. Global distributions of the tropospheric NO₂ columns (in 10^{15} mol cm⁻²), averaged over the 16–30 of each month, obtained from the CHASER simulation (w/o data assimilation, left columns), the data assimilation run (center columns), and DOMINO v2 (right columns) in January, April, July, and October 2005.

Global NO_x
emissions

K. Miyazaki et al.

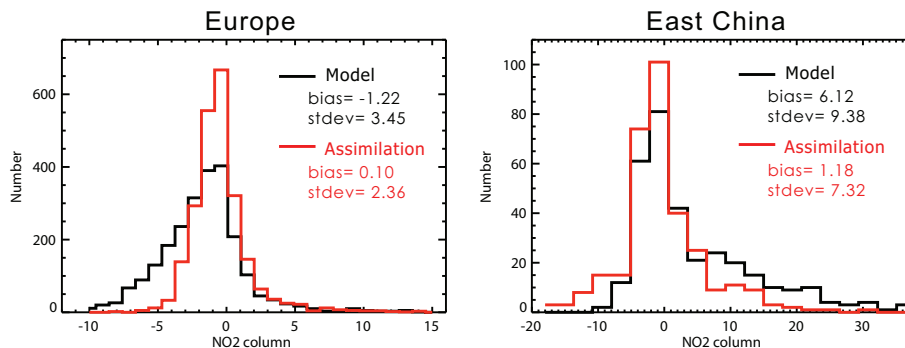


Fig. 10. Observation minus forecast (OmF) distributions of tropospheric NO₂ columns (in 10¹⁵ mol cm⁻²) calculated from the model simulation (black line) and the data assimilation run (red line) over Europe (10° W–30° E, 35–60° N, left panel) and Eastern China (110–123° E, 30–44° N, right panel) for the period 16–30 January 2005. The numbers shown in the figures are the mean value (bias) and the standard deviation (stdev) of the OmF in 10¹⁵ mol cm⁻² for the model simulation (black) and for the assimilation run (red).

[Title Page](#)
[Abstract](#)
[Introduction](#)
[Conclusions](#)
[References](#)
[Tables](#)
[Figures](#)
[◀](#)
[▶](#)
[◀](#)
[▶](#)
[Back](#)
[Close](#)
[Full Screen / Esc](#)
[Printer-friendly Version](#)
[Interactive Discussion](#)


Global NO_x
emissions

K. Miyazaki et al.

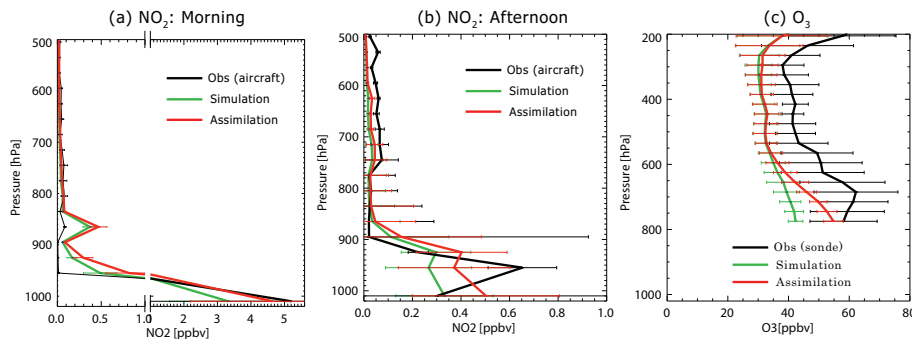


Fig. 11. Vertical profiles of the NO₂ concentrations (in ppbv) in (a, left panel) the morning (8–10 a.m.) and (b, center panel) the afternoon (2–4 p.m.) and (c, right panel) the O₃ concentrations (in ppbv) obtained during the INTEX-B campaign in March 2006. The black lines represent the observed profile; the green lines represent the model simulation; the red line represents the data assimilation run. The error bars represent the standard deviation of all the data within one grid cell.

[Title Page](#)[Abstract](#)[Introduction](#)[Conclusions](#)[References](#)[Tables](#)[Figures](#)[◀](#)[▶](#)[◀](#)[▶](#)[Back](#)[Close](#)[Full Screen / Esc](#)[Printer-friendly Version](#)[Interactive Discussion](#)

Global NO_x
emissions

K. Miyazaki et al.

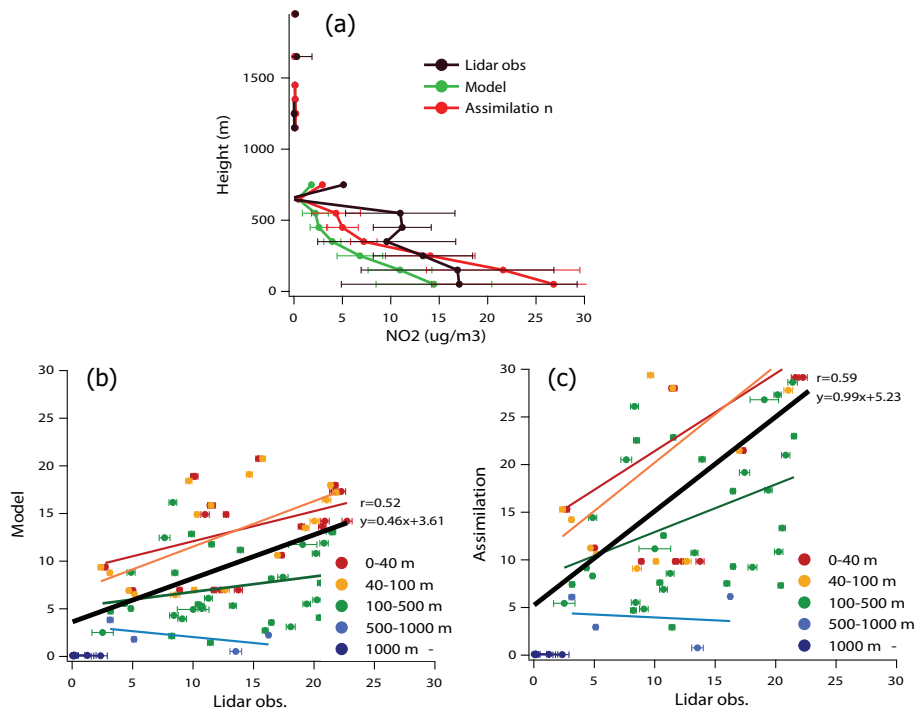


Fig. 12. (a, top panel) Mean vertical profiles of the NO₂ concentrations ($\mu\text{g m}^{-3}$) obtained during the DANDELIONS campaign in September 2006. The black lines represent the lidar observation; the green lines represent the model simulation; the red line represents the data assimilation run. The error bars represent the standard deviation of all the data within one grid. Lower panels show scatter plots of NO₂ concentrations ($\mu\text{g m}^{-3}$) for (b) the model simulation and (c) the data assimilation run during the DANDELIONS campaign. The straight lines represent linear regression lines for each level.

Title Page

Abstract

Introduction

Conclusions

References

Tables

Figures

◀

▶

◀

▶

Back

Close

Full Screen / Esc

Printer-friendly Version

Interactive Discussion



Global NO_x
emissions

K. Miyazaki et al.

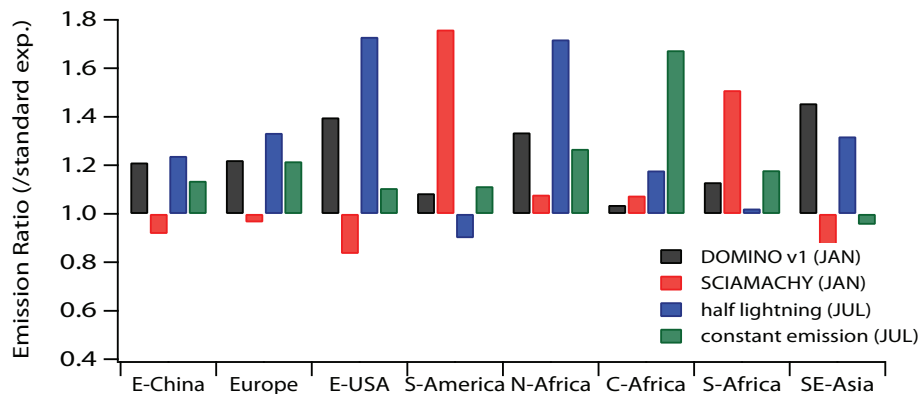


Fig. 13. Ratios of the regional mean NO_x emissions between the standard assimilation experiments using the DOMINO v2 observations and experiments conducted using different satellite products: the DOMINO v1 retrieval (black bars) and the SCIAMACHY retrieval (red bars) in January. Also shown are the emission ratios between the standard assimilation experiments and experiments conducted using different model settings: a 50 % reduction of NO_x emissions by lightning (blue bars) and without the diurnal variability scheme for the surface emissions (green bars) in July.

Title Page

Abstract

Introduction

Conclusions

References

Tables

Figures

◀

▶

◀

▶

Back

Close

Full Screen / Esc

Printer-friendly Version

Interactive Discussion

